Time-dependent amplitude analysis of $B^0 \to K^0_S \pi^+ \pi^-$

B. Aubert,[1] Y. Karyotakis,[1] J. P. Lees,[1] V. Poireau,[1] E. Prencipe,[1] X. Prudent,[1] V. Tisserand,[1] J. Garra Tico,[2] E. Grauges,[2] M. Martinelli,[3a,3b] A. Palano,[3a,3b] M. Pappagallo,[3a,3b] G. Eigen,[4] B. Stugu,[4] L. Sun,[4] M. Battaglia,[5] D. N. Brown,[5] L. T. Kerth,[5] Yu. G. Kolomensky,[5] G. Lynch,[5] I. L. Osipenkov,[5] K. Tackmann,[5] T. Tanabe,[5] C. M. Hawkes,[6] N. Soni,[6] A. T. Watson,[6] H. Koch,[7] T. Schroeder,[7] D. J. Asgeirsson,[8] B. G. Fulsom,[8] C. Hearty,[8] T. S. Mattison,[8] J. A. McKenna,[8] M. Barrett,[9] A. Khan,[9] A. Randle-Conde,[9] V. E. Blinov,[10] A. D. Bukin,[10,*] A. R. Buzykaev,[10] V. P. Druzhinin,[10] V. B. Golubev,[10] A. P. Onuchin,[10] S. I. Serednyakov,[10] Yu. I. Skovpen,[10] E. P. Solodov,[10] K. Yu. Todyshev,[10] M. Bondioli,[11] S. Curry,[11] I. Eschrich,[11] D. Kirkby,[11] A. J. Lankford,[11] P. Lund,[11] M. Mandelkern,[11] E. C. Martin,[11] D. P. Stoker,[11] S. Abachi,[12] C. Buchanan,[12] H. Atmacan,[13] J. W. Gary,[13] F. Liu,[13] O. Long,[13] G. M. Vitug,[13] Z. Yasin,[13] L. Zhang,[13] V. Sharma,[14] C. Campagnari,[15] T. M. Hong,[15] D. Kovalskyi,[15] M. A. Mazur,[15] J. D. Richman,[15] T. W. Beck,[16] A. M. Eisner,[16] C. A. Heusch,[16] J. Kroseberg,[16] W. S. Lockman,[16] A. J. Martinez,[16] T. Schalk,[16] B. A. Schumm,[16] A. Seiden,[16] L. O. Winstrom,[16] C. H. Cheng,[17] D. A. Doll,[17] B. Echenard,[17] F. Fang,[17] D. G. Hitlin,[17] I. Narsky,[17] T. Piatenko,[17] F. C. Porter,[17] R. Andreassen,[18] G. Mancinelli,[18] B. T. Meadows,[18] K. Mishra,[18] M. D. Sokoloff,[18] P. C. Bloom,[19] W. T. Ford,[19] A. Gaz,[19] J. F. Hirschauer,[19] M. Nagel,[19] U. Nauenberg,[19] J. G. Smith,[19] S. R. Wagner,[19] R. Ayad,[20,†] A. Soffer,[20,‡] W. H. Toki,[20] R. J. Wilson,[20] E. Feltresi,[21] A. Hauke,[21] H. Jasper,[21] T. M. Karbach,[21] J. Merkel,[21] A. Petzold,[21] B. Spaan,[21] K. Wacker,[21] M. J. Kobel,[22] R. Nogowski,[22] K. R. Schubert,[22] R. Schwierz,[22] A. Volk,[22] D. Bernard,[23] G. R. Bonneaud,[23] E. Latour,[23] M. Verderi,[23] P. J. Clark,[a24] S. Playfer,[a24] J. E. Watson,[a24] M. Andreotti,[25a,25b] D. Bettoni,[25a] C. Bozzi,[25a] R. Calabrese,[25a,25b] A. Cecchi,[25a,25b] G. Cibinetto,[25a,25b] E. Fioravanti,[25a,25b] P. Franchini,[25a,25b] E. Luppi,[25a,25b] M. Munerato,[25a,25b] M. Negrini,[25a,25b] A. Petrella,[25a,25b] L. Piemontese,[25a] V. Santoro,[25a,25b] R. Baldini-Ferroli,[26] A. Calcaterra,[26] R. de Sangro,[26] G. Finocchiaro,[26] S. Pacetti,[26] P. Patteri,[26] I. M. Peruzzi,[26,§] M. Piccolo,[26] M. Rama,[26] A. Zallo,[26] R. Contri,[27a,27b] E. Guido,[27a,27b] M. Lo Vetere,[27a,27b] M. R. Monge,[27a,27b] S. Passaggio,[27a] C. Patrignani,[27a,27b] E. Robutti,[27a] S. Tosi,[27a,27b] K. S. Chaisanguanthum,[28] M. Morii,[28] A. Adametz,[29] J. Marks,[29] S. Schenk,[29] U. Uwer,[29] F. U. Bernlochner,[30] V. Klose,[30] H. M. Lacker,[30] D. J. Bard,[31] P. D. Dauncey,[31] M. Tibbetts,[31] P. K. Behera,[32] M. J. Charles,[32] U. Mallik,[32] J. Cochran,[33] H. B. Crawley,[33] L. Dong,[33] V. Eyges,[33] W. T. Meyer,[33] S. Prell,[33] E. I. Rosenberg,[33] A. E. Rubin,[33] Y. Y. Gao,[34] A. V. Gritsan,[34] Z. J. Guo,[34] N. Arnaud,[35] J. Béquilleux,[35] A. D'Orazio,[35] M. Davier,[35] D. Derkach,[35] J. Firmino da Costa,[35] G. Grosdidier,[35] F. Le Diberder,[35] V. Lepeltier,[35] A. M. Lutz,[35] B. Malaescu,[35] S. Pruvot,[35] P. Roudeau,[35] M. H. Schune,[35] J. Serrano,[35] V. Sordini,[35,‖] A. Stocchi,[35] G. Wormser,[35] D. J. Lange,[36] D. M. Wright,[36] I. Bingham,[37] J. P. Burke,[37] C. A. Chavez,[37] J. R. Fry,[37] E. Gabathuler,[37] R. Gamet,[37] D. E. Hutchcroft,[37] D. J. Payne,[37] C. Touramanis,[37] A. J. Bevan,[38] C. K. Clarke,[38] F. Di Lodovico,[38] R. Sacco,[38] M. Sigamani,[38] G. Cowan,[39] S. Paramesvaran,[39] A. C. Wren,[39] D. N. Brown,[40] C. L. Davis,[40] A. G. Denig,[41] M. Fritsch,[41] W. Gradl,[41] A. Hafner,[41] K. E. Alwyn,[42] D. Bailey,[42] R. J. Barlow,[42] G. Jackson,[42] G. D. Lafferty,[42] T. J. West,[42] J. I. Yi,[42] J. Anderson,[43] C. Chen,[43] A. Jawahery,[43] D. A. Roberts,[43] G. Simi,[43] J. M. Tuggle,[43] C. Dallapiccola,[44] E. Salvati,[44] S. Saremi,[44] R. Cowan,[45] D. Dujmic,[45] P. H. Fisher,[45] S. W. Henderson,[45] G. Sciolla,[45] M. Spitznagel,[45] R. K. Yamamoto,[45] M. Zhao,[45] P. M. Patel,[46] S. H. Robertson,[46] M. Schram,[46] A. Lazzaro,[47a,47b] V. Lombardo,[47a] F. Palombo,[47a,47b] S. Stracka,[47a,47b] J. M. Bauer,[48] L. Cremaldi,[48] R. Godang,[48,¶] R. Kroeger,[48] D. J. Summers,[48] H. W. Zhao,[48] M. Simard,[49] P. Taras,[49] H. Nicholson,[50] G. De Nardo,[51a,51b] L. Lista,[51a] D. Monorchio,[51a,51b] G. Onorato,[51a,51b] C. Sciacca,[51a,51b] G. Raven,[52] H. L. Snoek,[52] C. P. Jessop,[53] K. J. Knoepfel,[53] J. M. LoSecco,[53] W. F. Wang,[53] L. A. Corwin,[54] K. Honscheid,[54] H. Kagan,[54] R. Kass,[54] J. P. Morris,[54] A. M. Rahimi,[54] J. J. Regensburger,[54] S. J. Sekula,[54] Q. K. Wong,[54] N. L. Blount,[55] J. Brau,[55] R. Frey,[55] O. Igonkina,[55] J. A. Kolb,[55] M. Lu,[55] R. Rahmat,[55] N. B. Sinev,[55] D. Strom,[55] J. Strube,[55] E. Torrence,[55] G. Castelli,[56a,56b] N. Gagliardi,[56a,56b] M. Margoni,[56a,56b] M. Morandin,[56a] M. Posocco,[56a] M. Rotondo,[56a] F. Simonetto,[56a,56b] R. Stroili,[56a,56b] C. Voci,[56a,56b] P. del Amo Sanchez,[57] E. Ben-Haim,[57] H. Briand,[57] J. Chauveau,[57] O. Hamon,[57] Ph. Leruste,[57] G. Marchiori,[57] J. Ocariz,[57] A. Perez,[57] J. Prendki,[57] S. Sitt,[57] L. Gladney,[58] M. Biasini,[59a,59b] E. Manoni,[59a,59b] C. Angelini,[60a,60b] G. Batignani,[60a,60b] S. Bettarini,[60a,60b] G. Calderini,[60a,60b,**] M. Carpinelli,[60a,60b,††] A. Cervelli,[60a,60b] F. Forti,[60a,60b] M. A. Giorgi,[60a,60b] A. Lusiani,[60a,60c] M. Morganti,[60a,60b] N. Neri,[60a,60b] E. Paoloni,[60a,60b] G. Rizzo,[60a,60b] J. J. Walsh,[60a] D. Lopes Pegna,[61] C. Lu,[61] J. Olsen,[61] A. J. S. Smith,[61] A. V. Telnov,[61] F. Anulli,[62a] E. Baracchini,[62a,62b] G. Cavoto,[62a] R. Faccini,[62a,62b] F. Ferrarotto,[62a] F. Ferroni,[62a,62b] M. Gaspero,[62a,62b] P. D. Jackson,[62a] L. Li Gioi,[62a] M. A. Mazzoni,[62a] S. Morganti,[62a] G. Piredda,[62a] F. Renga,[62a,62b] C. Voena,[62a] M. Ebert,[63] T. Hartmann,[63] H. Schröder,[63] R. Waldi,[63] T. Adye,[64] B. Franek,[64] E. O. Olaiya,[64] F. F. Wilson,[64] S. Emery,[65] L. Esteve,[65] G. Hamel de Monchenault,[65] W. Kozanecki,[65] G. Vasseur,[65] Ch. Yèche,[65] M. Zito,[65] M. T. Allen,[66] D. Aston,[66] R. Bartoldus,[66] J. F. Benitez,[66] R. Cenci,[66] J. P. Coleman,[66]

M. R. Convery,[66] J. C. Dingfelder,[66] J. Dorfan,[66] G. P. Dubois-Felsmann,[66] W. Dunwoodie,[66] R. C. Field,[66] A. M. Gabareen,[66] M. T. Graham,[66] P. Grenier,[66] C. Hast,[66] W. R. Innes,[66] J. Kaminski,[66] M. H. Kelsey,[66] H. Kim,[66] P. Kim,[66] M. L. Kocian,[66] D. W. G. S. Leith,[66] S. Li,[66] B. Lindquist,[66] S. Luitz,[66] V. Luth,[66] H. L. Lynch,[66] D. B. MacFarlane,[66] H. Marsiske,[66] R. Messner,[66,*] D. R. Muller,[66] H. Neal,[66] S. Nelson,[66] C. P. O'Grady,[66] I. Ofte,[66] M. Perl,[66] B. N. Ratcliff,[66] A. Roodman,[66] A. A. Salnikov,[66] R. H. Schindler,[66] J. Schwiening,[66] A. Snyder,[66] D. Su,[66] M. K. Sullivan,[66] K. Suzuki,[66] S. K. Swain,[66] J. M. Thompson,[66] J. Va'vra,[66] A. P. Wagner,[66] M. Weaver,[66] C. A. West,[66] W. J. Wisniewski,[66] M. Wittgen,[66] D. H. Wright,[66] H. W. Wulsin,[66] A. K. Yarritu,[66] K. Yi,[66] C. C. Young,[66] V. Ziegler,[66] X. R. Chen,[67] H. Liu,[67] W. Park,[67] M. V. Purohit,[67] R. M. White,[67] J. R. Wilson,[67] P. R. Burchat,[68] A. J. Edwards,[68] T. S. Miyashita,[68] S. Ahmed,[69] M. S. Alam,[69] J. A. Ernst,[69] B. Pan,[69] M. A. Saeed,[69] S. B. Zain,[69] S. M. Spanier,[70] B. J. Wogsland,[70] R. Eckmann,[71] J. L. Ritchie,[71] A. M. Ruland,[71] C. J. Schilling,[71] R. F. Schwitters,[71] B. C. Wray,[71] B. W. Drummond,[72] J. M. Izen,[72] X. C. Lou,[72] F. Bianchi,[73a,73b] D. Gamba,[73a,73b] M. Pelliccioni,[73a,73b] M. Bomben,[74a,74b] L. Bosisio,[74a,74b] C. Cartaro,[74a,74b] G. Della Ricca,[74a,74b] L. Lanceri,[74a,74b] L. Vitale,[74a,74b] V. Azzolini,[75] N. Lopez-March,[75] F. Martinez-Vidal,[75] D. A. Milanes,[75] A. Oyanguren,[75] J. Albert,[76] Sw. Banerjee,[76] B. Bhuyan,[76] H. H. F. Choi,[76] K. Hamano,[76] G. J. King,[76] R. Kowalewski,[76] M. J. Lewczuk,[76] I. M. Nugent,[76] J. M. Roney,[76] R. J. Sobie,[76] T. J. Gershon,[77] P. F. Harrison,[77] J. Ilic,[77] T. E. Latham,[77] G. B. Mohanty,[77] E. M. T. Puccio,[77] H. R. Band,[78] X. Chen,[78] S. Dasu,[78] K. T. Flood,[78] Y. Pan,[78] R. Prepost,[78] C. O. Vuosalo,[78] and S. L. Wu[78]

(*BABAR* Collaboration)

[1]*Laboratoire d'Annecy-le-Vieux de Physique des Particules (LAPP), Université de Savoie, CNRS/IN2P3, F-74941 Annecy-Le-Vieux, France*
[2]*Universitat de Barcelona, Facultat de Fisica, Departament ECM, E-08028 Barcelona, Spain*
[3a]*INFN Sezione di Bari, I-70126 Bari, Italy*
[3b]*Dipartimento di Fisica, Università di Bari, I-70126 Bari, Italy*
[4]*University of Bergen, Institute of Physics, N-5007 Bergen, Norway*
[5]*Lawrence Berkeley National Laboratory and University of California, Berkeley, California 94720, USA*
[6]*University of Birmingham, Birmingham, B15 2TT, United Kingdom*
[7]*Ruhr Universität Bochum, Institut für Experimentalphysik 1, D-44780 Bochum, Germany*
[8]*University of British Columbia, Vancouver, British Columbia, Canada V6T 1Z1*
[9]*Brunel University, Uxbridge, Middlesex UB8 3PH, United Kingdom*
[10]*Budker Institute of Nuclear Physics, Novosibirsk 630090, Russia*
[11]*University of California at Irvine, Irvine, California 92697, USA*
[12]*University of California at Los Angeles, Los Angeles, California 90024, USA*
[13]*University of California at Riverside, Riverside, California 92521, USA*
[14]*University of California at San Diego, La Jolla, California 92093, USA*
[15]*University of California at Santa Barbara, Santa Barbara, California 93106, USA*
[16]*University of California at Santa Cruz, Institute for Particle Physics, Santa Cruz, California 95064, USA*
[17]*California Institute of Technology, Pasadena, California 91125, USA*
[18]*University of Cincinnati, Cincinnati, Ohio 45221, USA*
[19]*University of Colorado, Boulder, Colorado 80309, USA*
[20]*Colorado State University, Fort Collins, Colorado 80523, USA*
[21]*Technische Universität Dortmund, Fakultät Physik, D-44221 Dortmund, Germany*
[22]*Technische Universität Dresden, Institut für Kern- und Teilchenphysik, D-01062 Dresden, Germany*
[23]*Laboratoire Leprince-Ringuet, CNRS/IN2P3, Ecole Polytechnique, F-91128 Palaiseau, France*
[a24]*University of Edinburgh, Edinburgh EH9 3JZ, United Kingdom*
[25a]*INFN Sezione di Ferrara, I-44100 Ferrara, Italy*
[25b]*Dipartimento di Fisica, Università di Ferrara, I-44100 Ferrara, Italy*
[26]*INFN Laboratori Nazionali di Frascati, I-00044 Frascati, Italy*
[27a]*INFN Sezione di Genova, I-16146 Genova, Italy*
[27b]*Dipartimento di Fisica, Università di Genova, I-16146 Genova, Italy*
[28]*Harvard University, Cambridge, Massachusetts 02138, USA*
[29]*Universität Heidelberg, Physikalisches Institut, Philosophenweg 12, D-69120 Heidelberg, Germany*
[30]*Humboldt-Universität zu Berlin, Institut für Physik, Newtonstr. 15, D-12489 Berlin, Germany*
[31]*Imperial College London, London, SW7 2AZ, United Kingdom*
[32]*University of Iowa, Iowa City, Iowa 52242, USA*
[33]*Iowa State University, Ames, Iowa 50011-3160, USA*
[34]*Johns Hopkins University, Baltimore, Maryland 21218, USA*

[35]Laboratoire de l'Accélérateur Linéaire, IN2P3/CNRS et Université Paris-Sud 11, Centre Scientifique d'Orsay, B. P. 34, F-91898 Orsay Cedex, France
[36]Lawrence Livermore National Laboratory, Livermore, California 94550, USA
[37]University of Liverpool, Liverpool L69 7ZE, United Kingdom
[38]Queen Mary, University of London, London, E1 4NS, United Kingdom
[39]University of London, Royal Holloway and Bedford New College, Egham, Surrey TW20 0EX, United Kingdom
[40]University of Louisville, Louisville, Kentucky 40292, USA
[41]Johannes Gutenberg-Universität Mainz, Institut für Kernphysik, D-55099 Mainz, Germany
[42]University of Manchester, Manchester M13 9PL, United Kingdom
[43]University of Maryland, College Park, Maryland 20742, USA
[44]University of Massachusetts, Amherst, Massachusetts 01003, USA
[45]Massachusetts Institute of Technology, Laboratory for Nuclear Science, Cambridge, Massachusetts 02139, USA
[46]McGill University, Montréal, Québec, Canada H3A 2T8
[47a]INFN Sezione di Milano, I-20133 Milano, Italy
[47b]Dipartimento di Fisica, Università di Milano, I-20133 Milano, Italy
[48]University of Mississippi, University, Mississippi 38677, USA
[49]Université de Montréal, Physique des Particules, Montréal, Québec, Canada H3C 3J7
[50]Mount Holyoke College, South Hadley, Massachusetts 01075, USA
[51a]INFN Sezione di Napoli, I-80126 Napoli, Italy
[51b]Dipartimento di Scienze Fisiche, Università di Napoli Federico II, I-80126 Napoli, Italy
[52]NIKHEF, National Institute for Nuclear Physics and High Energy Physics, NL-1009 DB Amsterdam, The Netherlands
[53]University of Notre Dame, Notre Dame, Indiana 46556, USA
[54]Ohio State University, Columbus, Ohio 43210, USA
[55]University of Oregon, Eugene, Oregon 97403, USA
[56a]INFN Sezione di Padova, I-35131 Padova, Italy
[56b]Dipartimento di Fisica, Università di Padova, I-35131 Padova, Italy
[57]Laboratoire de Physique Nucléaire et de Hautes Energies, IN2P3/CNRS, Université Pierre et Marie Curie-Paris6, Université Denis Diderot-Paris7, F-75252 Paris, France
[58]University of Pennsylvania, Philadelphia, Pennsylvania 19104, USA
[59a]INFN Sezione di Perugia, I-06100 Perugia, Italy
[59b]Dipartimento di Fisica, Università di Perugia, I-06100 Perugia, Italy
[60a]INFN Sezione di Pisa, I-56127 Pisa, Italy
[60b]Dipartimento di Fisica, Università di Pisa, I-56127 Pisa, Italy
[60c]Scuola Normale Superiore di Pisa, I-56127 Pisa, Italy
[61]Princeton University, Princeton, New Jersey 08544, USA
[62a]INFN Sezione di Roma, I-00185 Roma, Italy
[62b]Dipartimento di Fisica, Università di Roma La Sapienza, I-00185 Roma, Italy
[63]Universität Rostock, D-18051 Rostock, Germany
[64]Rutherford Appleton Laboratory, Chilton, Didcot, Oxon, OX11 0QX, United Kingdom
[65]CEA, Irfu, SPP, Centre de Saclay, F-91191 Gif-sur-Yvette, France
[66]SLAC National Accelerator Laboratory, Stanford, California 94309 USA
[67]University of South Carolina, Columbia, South Carolina 29208, USA
[68]Stanford University, Stanford, California 94305-4060, USA
[69]State University of New York, Albany, New York 12222, USA
[70]University of Tennessee, Knoxville, Tennessee 37996, USA
[71]University of Texas at Austin, Austin, Texas 78712, USA
[72]University of Texas at Dallas, Richardson, Texas 75083, USA
[73a]INFN Sezione di Torino, I-10125 Torino, Italy
[73b]Dipartimento di Fisica Sperimentale, Università di Torino, I-10125 Torino, Italy

[*]Deceased.
[†]Now at Temple University, Philadelphia, Pennsylvania 19122, USA.
[‡]Now at Tel Aviv University, Tel Aviv, 69978, Israel.
[§]Also with Università di Perugia, Dipartimento di Fisica, Perugia, Italy.
[‖]Also with Università di Roma La Sapienza, I-00185 Roma, Italy.
[¶]Now at University of South Alabama, Mobile, Alabama 36688, USA.
[**]Also with Laboratoire de Physique Nucléaire et de Hautes Energies, IN2P3/CNRS, Université Pierre et Marie Curie-Paris6, Université Denis Diderot-Paris7, F-75252 Paris, France.
[††]Also with Università di Sassari, Sassari, Italy.

[74a]*INFN Sezione di Trieste; I-34127 Trieste, Italy*
[74b]*Dipartimento di Fisica, Università di Trieste, I-34127 Trieste, Italy*
[75]*IFIC, Universitat de Valencia-CSIC, E-46071 Valencia, Spain*
[76]*University of Victoria, Victoria, British Columbia, Canada V8W 3P6*
[77]*Department of Physics, University of Warwick, Coventry CV4 7AL, United Kingdom*
[78]*University of Wisconsin, Madison, Wisconsin 53706, USA*
(Received 25 May 2009; published 2 December 2009)

We perform a time-dependent amplitude analysis of $B^0 \to K^0_S\pi^+\pi^-$ decays to extract the *CP* violation parameters of $f_0(980)K^0_S$ and $\rho^0(770)K^0_S$ and the direct *CP* asymmetry of $K^{*+}(892)\pi^-$. The results are obtained from a data sample of $(383 \pm 3) \times 10^6$ $B\bar{B}$ decays, collected with the *BABAR* detector at the PEP-II asymmetric–energy *B* factory at SLAC. We find two solutions, with an equivalent goodness-of-fit. Including systematic and Dalitz plot model uncertainties, the combined confidence interval for values of the *CP* parameter $\beta_{\rm eff}$ in B^0 decays to $f_0(980)K^0_S$ is $18° < \beta_{\rm eff} < 76°$ at 95% confidence level (C.L). *CP* conservation in B^0 decays to $f_0(980)K^0_S$ is excluded at 3.5 standard deviations including systematic uncertainties. For B^0 decays to $\rho^0(770)K^0_S$, the combined confidence interval is $-9° < \beta_{\rm eff} < 57°$ at 95% C.L. In decays to $K^{*+}(892)\pi^-$ we measure the direct *CP* asymmetry to be $A_{CP} = -0.20 \pm 0.10 \pm 0.01 \pm 0.02$. The measured phase difference (including $B^0\bar{B}^0$ mixing) between decay amplitudes of $B^0 \to K^{*+}(892)\pi^-$ and $\bar{B}^0 \to K^{*-}(892)\pi^+$, excludes the interval $-137° < \Delta\Phi(K^{*+}(892)\pi^-) < -5°$ at 95% C.L.

DOI: 10.1103/PhysRevD.80.112001 PACS numbers: 13.66.Bc, 13.25.Gv, 13.25.Jx, 14.40.Cs

I. INTRODUCTION

The Cabibbo-Kobayashi-Maskawa (CKM) mechanism [1,2] for quark mixing describes all transitions between quarks in terms of only four parameters: three rotation angles and one irreducible phase. Consequently, the flavor sector of the standard model (SM) is highly predictive. One particularly interesting prediction is that mixing-induced *CP* asymmetries in decays governed by $b \to q\bar{q}s$ ($q = u$, d, s) transitions are, to a good approximation, the same as those found in $b \to c\bar{c}s$ transitions. Since flavor changing neutral currents are forbidden at tree-level in the standard model, the $b \to s$ transition proceeds via loop diagrams (penguins), which are affected by new particles in many extensions of the SM.

Various $b \to s$ dominated charmless hadronic *B* decays have been studied in order to probe this prediction. The values of the mixing-induced *CP* asymmetry measured for each (quasi-)two-body mode can be compared to that measured in $b \to c\bar{c}s$ transitions (typically using $B^0 \to J/\psi K^0_S$). A recent compilation [3] of results shows that they tend to have central values below that for $b \to c\bar{c}s$. Recent theoretical evaluations [4–12] suggest that SM corrections to the $b \to q\bar{q}s$ mixing-induced *CP* violation parameters should be small, in particular, for the modes ϕK^0, $\eta' K^0$, and $K^0_S K^0_S K^0_S$, and tend to *increase* the values, i.e. the opposite trend to that seen in the data. However, there is currently no convincing evidence for new physics effects in these transitions. Clearly, more precise experimental results are required.

The compilation given in [3] includes several three-body modes, which may be used either by virtue of being *CP* eigenstates ($K^0_S K^0_S K^0_S$, $K^0_S\pi^0\pi^0$) [13] or because their *CP* content can be determined experimentally ($K^+K^-K^0$) [14,15]. It also includes quasi-two-body (Q2B) modes, such as $f_0(980)K^0_S$ and $\rho^0(770)K^0_S$, which are reconstructed via their three-body final states ($K^0_S\pi^+\pi^-$ for these modes). The precision of the Q2B approach is limited as other structures in the phase space may cause interference with the resonances considered as signal. Therefore, more precise results can be obtained using a time-dependent amplitude analysis covering the complete phase space, or Dalitz plot (DP), of $B^0 \to K^0_S\pi^+\pi^-$. Furthermore, the interference terms allow the cosine of the effective weak phase difference in mixing and decay to be determined, helping to resolve ambiguities which arise from the Q2B analysis. This approach has been successfully used in a time-dependent DP analysis of $B^0 \to K^+K^-K^0$ [15].

The discussion above assumes that the $b \to s$ penguin amplitude dominates the decay. However, for each mode contributing to the $K^0_S\pi^+\pi^-$ final state, there is also the possibility of a $b \to u$ tree diagram. These are doubly CKM suppressed compared to the $b \to s$ penguin diagram (the tree is $\mathcal{O}(\lambda^4)$, whereas the penguin is $\mathcal{O}(\lambda^2)$, where λ is the usual Wolfenstein parameter [16,17]). However, hadronic factors may enhance the tree amplitudes, resulting in a significant ''tree pollution.'' These hadronic factors may be different for each Q2B state, thus the relative magnitudes of each tree and penguin amplitudes, $|T/P|$, and the strong phase difference may be different as well. Nonetheless, the relative weak phase between these two amplitudes is the same—and in the standard model is equal to the CKM unitarity triangle angle γ. An amplitude analysis, in contrast to a Q2B analysis, yields sufficient information to extract relative phases and magnitudes. Measurements of decay amplitudes in the DP analysis of $B^0 \to K^0_S\pi^+\pi^-$ (and similar modes) can therefore be used to set constraints on the CKM parameters $(\bar{\rho}, \bar{\eta})$ [18–21].

Recently published results on time-dependent DP analysis of $B^0 \to K^0_S\pi^+\pi^-$ are available [22]. Previous studies of the $B^0 \to K^0_S\pi^+\pi^-$ decay were either based on a Q2B approach [23], or were amplitude analyses that did not take into account either time-dependence or flavor-tag dependence [24]. The available results for $B^0 \to K^0_S\pi^+\pi^-$ are consistent with studies obtained from other $B \to K\pi\pi$ decay modes: $K^+\pi^-\pi^0$ [25,26] and $K^+\pi^+\pi^-$ [27,28]. The latter results indicate evidence for direct CP violation in the $B^+ \to \rho^0(770)K^+$ channel. If confirmed, this will be the first observation of CP violation in the decay of any charged particle. The relevance of $B \to K\pi\pi$ is further highlighted by recent theoretical calculations [29] suggesting that large CP violation effects are expected in several $B \to K^*\pi$ and $B \to K\rho$ resonant modes.

In this paper we present results from a time-dependent amplitude analysis of the $B^0 \to K^0_S\pi^+\pi^-$ decay. In Sec. II we describe the time-dependent DP formalism, and introduce the signal parameters that are extracted in the fit to data. In Sec. III we briefly describe the *BABAR* detector and the data set. In Sec. IV, we explain the selection requirements used to obtain the signal candidates and suppress backgrounds. In Sec. V we describe the fit method and the approach used to control experimental effects such as resolution. In Sec. VI we present the results of the fit, and extract parameters relevant to the contributing intermediate resonant states. In Sec. VII we discuss systematic uncertainties in the results, and finally we summarize the results in Sec. VIII.

II. ANALYSIS OVERVIEW

Taking advantage of the interference pattern in the DP, we measure relative magnitudes and phases for the different resonant decay modes using a maximum-likelihood fit. Below, we detail the formalism used in the present analysis.

A. Decay amplitudes

We consider the decay of a spin-zero B^0 with four-momentum p_B into the three daughters π^+, π^-, and K^0_S with p_+, p_-, and p_0 their corresponding four-momenta. Using as independent (Mandelstam) variables the invariant squared masses

$$\begin{aligned} s_+ &= m^2_{K^0_S\pi^+} = (p_+ + p_0)^2, \\ s_- &= m^2_{K^0_S\pi^-} = (p_- + p_0)^2, \end{aligned} \tag{1}$$

the invariant squared mass $s_0 = m^2_{\pi^+\pi^-} = (p_+ + p_-)^2$ can be obtained from energy and momentum conservation:

$$s_0 = m^2_{B^0} + 2m^2_{\pi^+} + m^2_{K^0_S} - s_+ - s_-. \tag{2}$$

The differential B^0 decay width with respect to the variables defined in Eq. (1) (i.e. the Dalitz plot) reads

$$d\Gamma(B^0 \to K^0_S\pi^+\pi^-) = \frac{1}{(2\pi)^3}\frac{|\mathcal{A}|^2}{32m^3_{B^0}}ds_+ds_-, \tag{3}$$

where $\mathcal{A}$ is the Lorentz-invariant amplitude of the three-body decay. In the following, the amplitudes $\mathcal{A}$ and $\bar{\mathcal{A}}$ correspond to the transitions $B^0 \to K^0_S\pi^+\pi^-$ and $\bar{B}^0 \to K^0_S\pi^+\pi^-$, respectively. We describe the distribution of signal events in the DP using an isobar approximation, which models the total amplitude as resulting from a coherent sum of amplitudes from the N individual decay channels

$$\mathcal{A}(s_+, s_-) = \sum_{j=1}^{N} c_j F_j(s_+, s_-), \tag{4}$$

$$\bar{\mathcal{A}}(s_+, s_-) = \sum_{j=1}^{N} \bar{c}_j \bar{F}_j(s_+, s_-), \tag{5}$$

where F_j are DP-dependent dynamical amplitudes described below, and c_j complex coefficients describing the relative magnitude and phase of the different decay channels. All the weak phase dependence is contained in c_j, and F_j contains strong dynamics only; therefore,

$$F_j(s_+, s_-) = \bar{F}_j(s_-, s_+). \tag{6}$$

The resonance dynamics are contained within the F_j terms, which are represented by the product of the invariant mass and angular distribution probabilities, i.e.,

$$F^L_j(s_+, s_-) = R_j(m)X_L(|\vec{p}^\star|r')X_L(|\vec{q}|r)T_j(L, \vec{p}, \vec{q}) \tag{7}$$

where

(i) m is the invariant mass of the decay products of the resonance,
(ii) $R_j(m)$ is the resonance mass term or "line shape" (e.g. Breit–Wigner),
(iii) L is the orbital angular momentum between the resonance and the bachelor particle,
(iv) $\vec{p}^\star$ is the momentum of the bachelor particle evaluated in the rest frame of the B,
(v) $\vec{p}$ and $\vec{q}$ are the momenta of the bachelor particle and one of the resonance daughters, respectively, both evaluated in the rest frame of the resonance (for $K^0_S\pi^-$, $K^0_S\pi^+$, and $\pi^+\pi^-$ resonances, $\vec{q}$ is assigned to the momentum of the K^0_S, π^+, and π^-, respectively),
(vi) X_L are Blatt–Weisskopf barrier factors [30] with parameters r' (taken to be 2 $(\mathrm{GeV}/c)^{-1}$) and r (given in Table I), and
(vii) $T_j(L, \vec{p}, \vec{q})$ is the angular distribution:

$$L = 0: \quad T_j = 1, \tag{8}$$

$$L = 1: \quad T_j = -4\vec{p}\cdot\vec{q}, \tag{9}$$

$$L = 2: \quad T_j = \frac{8}{3}[3(\vec{p}\cdot\vec{q})^2 - (|\vec{p}||\vec{q}|)^2]. \tag{10}$$

TABLE I. Parameters of the DP model used in the fit. Values are given in MeV/(c^2), unless mentioned otherwise. The mass and width for the $f_X(1300)$ are averaged from results in $B^+ \to K^+\pi^-\pi^+$ Dalitz analyses [27,28].

Resonance	Parameters	Line shape	Ref. for Parameters
$f_0(980)$	$m_0 = 965 \pm 10$ $g_\pi = 165 \pm 18$ $g_K = 695 \pm 93$	Flatté	[31]
$\rho^0(770)$	$m_0 = 775.5 \pm 0.4$ $\Gamma_0 = 146.4 \pm 1.1$ $r = 5.3^{+0.9}_{-0.7}$ (GeV/c)$^{-1}$	GS	[32]
$K^{*+}(892)$ $K^{*-}(892)$	$m_0 = 891.66 \pm 0.26$ $\Gamma_0 = 50.8 \pm 0.9$ $r = 3.6 \pm 0.6$ (GeV/c)$^{-1}$	RBW	[32]
$(K\pi)_0^{*+}$ $(K\pi)_0^{*-}$	$m_0 = 1415 \pm 3$ $\Gamma_0 = 300 \pm 6$ $m_{K\pi}^{\text{cutoff}} = 1800$ $a = 2.07 \pm 0.10$ (GeV/c)$^{-1}$ $r = 3.32 \pm 0.34$ (GeV/c)$^{-1}$	LASS	[27]
$f_2(1270)$	$m_0 = 1275.4 \pm 1.1$ $\Gamma_0 = 185.2^{+3.1}_{-2.5}$ $r = 3.0$ (GeV/c)$^{-1}$	RBW	[32]
$f_X(1300)$	$m_0 = 1471 \pm 7$ $\Gamma_0 = 97 \pm 15$	RBW	[27,28]
NR decays		flat phase space	
χ_{c0}	$m_0 = 3414.75 \pm 0.35$ $\Gamma_0 = 10.4 \pm 0.7$	RBW	[32]

The helicity angle of a resonance is defined as the angle between $\vec{p}$ and $\vec{q}$. Explicitly, for $K_S^0\pi^-$, $K_S^0\pi^+$, and $\pi^+\pi^-$ resonances the helicity angle is defined between the momenta of the bachelor particle and of the K_S^0, π^+, and π^-, respectively, in the resonance rest frame.

For most resonances in this analysis the R_j are taken to be relativistic Breit–Wigner (RBW) [32] line shapes:

$$R_j(m) = \frac{1}{(m_0^2 - m^2) - im_0\Gamma(m)}, \tag{11}$$

where m_0 is the nominal mass of the resonance and $\Gamma(m)$ is the mass-dependent width. In the general case of a spin-J resonance, the latter can be expressed as

$$\Gamma(m) = \Gamma_0\left(\frac{q}{q_0}\right)^{2J+1}\left(\frac{m_0}{m}\right)\frac{X_J^2(q)}{X_J^2(q_0)}. \tag{12}$$

The symbol Γ_0 denotes the nominal width of the resonance. The values of m_0 and Γ_0 are listed in Table I. The symbol q_0 denotes the value of q when $m = m_0$.

For the $f_0(980)$ line shape the Flatté form [33] is used. In this case the mass-dependent width is given by the sum of the widths in the $\pi\pi$ and KK systems:

$$\Gamma(m) = \Gamma_{\pi\pi}(m) + \Gamma_{KK}(m), \tag{13}$$

where

$$\Gamma_{\pi\pi}(m) = g_\pi\left(\frac{1}{3}\sqrt{1 - 4m_{\pi^0}^2/m^2} + \frac{2}{3}\sqrt{1 - 4m_{\pi^\pm}^2/m^2}\right), \tag{14}$$

$$\Gamma_{KK}(m) = g_K\left(\frac{1}{2}\sqrt{1 - 4m_{K^\pm}^2/m^2} + \frac{1}{2}\sqrt{1 - 4m_{K^0}^2/m^2}\right). \tag{15}$$

The fractional coefficients arise from isospin conservation and g_π and g_K are coupling constants for which the values are given in Table I.

For the $\rho^0(770)$ we use the Gounaris–Sakurai (GS) parametrization [34], that describes the P-wave scattering amplitude for a broad resonance, decaying to two pions:

$$R_j(m) = \frac{1 + d\cdot\Gamma_0/m_0}{(m_0^2 - m^2) + f(m) - im_0\Gamma(m)}, \tag{16}$$

where

$$f(m) = \Gamma_0\frac{m_0^2}{q_0^3}\Big[q^2(h(m) - h(m_0)) + (m_0^2 - m^2)q_0^2\frac{dh}{dm^2}\Big|_{m=m_0}\Big], \tag{17}$$

and the function $h(m)$ is defined as

$$h(m) = \frac{2}{\pi}\frac{q}{m}\ln\left(\frac{m+2q}{2m_\pi}\right), \tag{18}$$

with

$$\left.\frac{dh}{dm^2}\right|_{m=m_0} = h(m_0)\left(\frac{1}{8q_0^2} - \frac{1}{2m_0^2}\right) + \frac{1}{2\pi m_0^2}. \tag{19}$$

The normalization condition at $R_j(0)$ fixes the parameter $d = f(0)/(\Gamma_0 m_0)$. It is found to be

$$d = \frac{3}{\pi}\frac{m_\pi^2}{q_0^2}\ln\left(\frac{m_0+2q_0}{2m_\pi}\right) + \frac{m_0}{2\pi q_0} - \frac{m_\pi^2 m_0}{\pi q_0^3}. \tag{20}$$

The 0^+ component of the $K\pi$ spectrum is not well understood [35,36]; we dub this component $(K\pi)_0^{*\pm}$ and use the LASS parametrization [35] which consists of the $K^*(1430)$ resonance together with an effective range nonresonant (NR) component:

$$R_j(m_{K\pi}) = \frac{m_{K\pi}}{q\cot\delta_B - iq} + e^{2i\delta_B}\frac{m_0\Gamma_0\frac{m_0}{q_0}}{(m_0^2 - m_{K\pi}^2) - im_0\Gamma_0\frac{q}{m_{K\pi}}\frac{m_0}{q_0}}, \tag{21}$$

where $\cot\delta_B = \frac{1}{aq} + \frac{1}{2}rq$. The values we have used for the scattering length (a) and effective range (r) parameters of this distribution are given in Table I. The effective range part of the amplitude is cut off at $m_{K\pi}^{\rm cutoff} = 1800\ {\rm MeV}/c^2$. Integrating separately the resonant part, the effective range part, and the coherent sum we find that the $K^*(1430)$ resonance accounts for 81.7%, the effective range term 44.1%, and destructive interference between the two terms is responsible for the excess 25.8%.

A flat phase-space term has been included in the signal model to account for NR $B^0 \to K_S^0\pi^+\pi^-$ decays.

We determine a nominal signal Dalitz-plot model using information from previous studies [23,24] and the change in the fit likelihood value observed when omitting or adding resonances. The components of the nominal signal model are summarized in Table I. Other components, taken into account only to estimate the DP model uncertainty, are discussed in Sec. VII.

B. Time dependence

With $\Delta t \equiv t_{\rm sig} - t_{\rm tag}$ defined as the proper time interval between the decay of the fully reconstructed $B^0 \to K_S^0\pi^+\pi^-$ ($B_{\rm sig}^0$) and that of the other meson ($B_{\rm tag}^0$) from the $\Upsilon(4S)$, the time-dependent decay rate $|\mathcal{A}_{\rm sig}^+(\Delta t)|^2$ ($|\mathcal{A}_{\rm sig}^-(\Delta t)|^2$) when the $B_{\rm tag}^0$ is a B^0 ($\bar{B}^0$) is given by

$$|\mathcal{A}_{\rm sig}^{\pm}(\Delta t)|^2 = \frac{e^{-|\Delta t|/\tau_{B^0}}}{4\tau_{B^0}}[|\mathcal{A}|^2 + |\bar{\mathcal{A}}|^2 \mp (|\mathcal{A}|^2 - |\bar{\mathcal{A}}|^2) \times \cos(\Delta m_d\Delta t) \pm 2{\rm Im}[\bar{\mathcal{A}}\,\mathcal{A}^*]\sin(\Delta m_d\Delta t)], \tag{22}$$

where τ_{B^0} is the neutral B meson lifetime and Δm_d is the $B^0\bar{B}^0$ mass difference. In the last formula and in the following, the DP dependence of the amplitudes is implicit. Here, we have assumed that there is no CP violation in mixing, and have used a convention whereby the phase from $B^0\bar{B}^0$ mixing is absorbed into the $\bar{B}^0$ decay amplitude (i.e. into the $\bar{c}_j$ terms). In other words, we assume that the $B^0\bar{B}^0$ mixing parameters satisfy $|q/p| = 1$ and absorb q/p into $\bar{c}_j$. Lifetime differences in the neutral B meson system are assumed to be negligible.

C. The square Dalitz plot

Both the signal events and the combinatorial $e^+e^- \to q\bar{q}$ ($q = u, d, s, c$) continuum background events populate the kinematic boundaries of the DP due to the low final state masses compared with the B^0 mass. The representation in Eq. (3) is inconvenient when empirical reference shapes are to be used. Large variations occurring in small areas of the DP are very difficult to describe in detail. We therefore apply the transformation

$$ds_+ ds_- \to |\det J| dm' d\theta', \tag{23}$$

which defines the square Dalitz plot (SDP). The new coordinates are

$$m' \equiv \frac{1}{\pi}\arccos\left(2\frac{m_0 - m_0^{\rm min}}{m_0^{\rm max} - m_0^{\rm min}} - 1\right), \qquad \theta' \equiv \frac{1}{\pi}\theta_0, \tag{24}$$

where $m_0 = \sqrt{s_0}$ is the $\pi^+\pi^-$ invariant mass, $m_0^{\rm max} = m_{B^0} - m_{K_S^0}$ and $m_0^{\rm min} = 2m_{\pi^+}$ are the kinematic limits of m_0, θ_0 is the $\pi^+\pi^-$ resonance helicity angle and J is the Jacobian of the transformation. Both variables range between 0 and 1. The determinant of the Jacobian is given by

$$|\det J| = 4|\mathbf{p}_+^*||\mathbf{p}_0^*|m_0 \cdot \frac{\partial m_0}{\partial m'} \cdot \frac{\partial\cos\theta_0}{\partial\theta'}, \tag{25}$$

where $|\mathbf{p}_+^*| = \sqrt{E_+^{*2} - m_{\pi^+}^2}$ and $|\mathbf{p}_0^*| = \sqrt{E_0^{*2} - m_{K_S^0}^2}$, and where the π^+ (K_S^0) energy E_+^* (E_0^*), is defined in the $\pi^+\pi^-$ rest frame. This transformation was introduced in Ref. [37], and has been used in several B decay DP analyses.

III. THE *BABAR* DETECTOR AND DATASET

The data used in this analysis were collected with the *BABAR* detector at the PEP-II asymmetric-energy e^+e^- storage ring at SLAC between October 1999 and August

2006. The sample consists of an integrated luminosity of 347.3 fb^{-1}, corresponding to $(383 \pm 3) \times 10^6$ $B\bar{B}$ pairs collected at the $\Upsilon(4S)$ resonance ("on-resonance"), and 36.6 fb^{-1} collected about 40 MeV below the $\Upsilon(4S)$("off-resonance").

A detailed description of the *BABAR* detector is presented in Ref. [38]. The tracking system used for track and vertex reconstruction has two components: a silicon vertex tracker (SVT) and a drift chamber (DCH), both operating within a 1.5 T magnetic field generated by a superconducting solenoidal magnet. Photons are identified in an electromagnetic calorimeter (EMC). It surrounds a detector of internally reflected Cherenkov light (DIRC), which associates Cherenkov photons with tracks for particle identification. Muon candidates are identified with the use of the instrumented flux return (IFR) of the solenoid.

IV. EVENT SELECTION AND BACKGROUNDS

We reconstruct $B^0 \to K^0_S\pi^+\pi^-$ candidates from pairs of oppositely-charged tracks and a $K^0_S \to \pi^+\pi^-$ candidate, which are required to form a good quality vertex. In order to ensure that all events are within the DP boundaries, we constrain the invariant mass of the final state to the B mass. For the $\pi^+\pi^-$ pair from the B, we use information from the tracking system, EMC, and DIRC to remove tracks consistent with electron, kaon, and proton hypotheses. In addition we require at least one track to be inconsistent with the muon hypothesis based on information from the IFR. The K^0_S candidate is required to have a mass within 15 MeV/c^2 of the nominal K^0 mass [32], and a lifetime significance of at least 5 standard deviations. The last requirement ensures that the decay vertices of the B^0 and the K^0_S are well separated. In addition, combinatorial background is suppressed by requiring the cosine of the angle between the K^0_S flight direction and the vector connecting the B-daughter pions and the K^0_S vertices to be greater than 0.999.

A B-meson candidate is characterized kinematically by the energy-substituted mass $m_{\rm ES} \equiv \sqrt{(s/2 + \mathbf{p}_i \cdot \mathbf{p}_B)^2/E_i^2 - p_B^2}$ and energy difference $\Delta E \equiv E_B^* - \frac{1}{2}\sqrt{s}$, where $(E_B, \mathbf{p}_B)$ and $(E_i, \mathbf{p}_i)$ are the four-vectors of the B-candidate and the initial electron-positron system, respectively. The asterisk denotes the $\Upsilon(4S)$ frame, and s is the square of the invariant mass of the electron-positron system. We require $5.272 < m_{\rm ES} < 5.286$ GeV/c^2 and $|\Delta E| < 0.065$ GeV. Following the calculation of these kinematic variables, each of the B candidates is refitted with its mass constrained to the world average value of the B-meson mass [32] in order to improve the DP position resolution, and ensure that Eq. (2) holds.

Backgrounds arise primarily from random combinations in continuum events. To enhance discrimination between signal and continuum, we use a neural network (NN) [39] to combine four discriminating variables: the angles with respect to the beam axis of the B momentum and B thrust axis in the $\Upsilon(4S)$ frame, and the zeroth and second order monomials $L_{0,2}$ of the energy flow about the B thrust axis. The monomials are defined by $L_n = \sum_i p_i \times |\cos\theta_i|^n$, where θ_i is the angle with respect to the B thrust axis of track or neutral cluster i and p_i is the magnitude of its momentum. The sum excludes the B candidate and all quantities are calculated in the $\Upsilon(4S)$ frame. The NN is trained using off-resonance data as well as simulated signal events, all of which passed the selection criteria. The final sample of signal candidates is selected with a requirement on the NN output that retains 90% of the signal and rejects 71% of the continuum.

The time difference Δt is obtained from the measured distance between the positions of the $B^0_{\rm sig}$ and $B^0_{\rm tag}$ decay vertices, using the boost $\beta\gamma = 0.56$ of the e^+e^- system. B^0 candidates with $|\Delta t| > 20$ ps are rejected, as are candidates for which the error on Δt is higher than 2.5 ps. To determine the flavor of $B^0_{\rm tag}$ we use the B flavor-tagging algorithm of Ref. [40]. This algorithm combines several different signatures, such as charges, momenta, and decay angles of charged particles in the event to achieve optimal separation between the two B flavors. This produces six mutually exclusive tagging categories: lepton, two different kaon categories, slow pion, kaon-slow pion, and a category that uses a combination of other signatures. We also retain untagged events in a seventh category since although these events do not contribute to the measurement of the time-dependent CP asymmetries they do provide additional statistics for the measurements of direct CP violation and CP-conserving quantities such as the branching fractions [41]. Multiple B candidates passing the full selection occur between $\sim$1% of the time for NR signal events and $\sim$8% of the time for $B^0 \to f_0(980)K^0_S$ signal events. If an event has more than one candidate, we select one using a reproducible pseudorandom procedure based on the event timestamp.

With the above selection criteria, we obtain a signal efficiency determined from Monte Carlo (MC) simulation of 21%–25%, depending on the position in the DP.

Of the selected signal events, 8% of $B^0 \to \rho^0 K^0_S$, 6% of $B^0 \to K^*(892)^+\pi^-$ and 4% of $B^0 \to f_0(980)K^0_S$ events are misreconstructed. Misreconstructed events occur when a track from the tagging B is assigned to the reconstructed signal candidate. This occurs most often for low-momentum tracks and hence the misreconstructed events are concentrated in the corners of the DP. Since these are also where the low-mass resonances overlap strongly with other resonances, it is important to model the misreconstructed events correctly. The model used to account for misreconstructed events is detailed in Sec. VA.

We use MC events to study the background from other B decays (B background). More than 50 channels were considered in preliminary studies, of which 20 are included in

TABLE II. Summary of B background modes included in the fit model. When the yield is varied in the fit, the quoted number of events corresponds to the fit results. Otherwise, the expected number, taking into account the branching ratios and efficiency, is given.

Mode	Varied	BR	Number of events
$B^0 \to D^-(\to K^0_S\pi^-)\pi^+$	yes	...	3377 ± 60
$B^0 \to J/\psi(\to l^+l^-)K^0_S$	yes	...	1803 ± 43
$B^0 \to \psi(2S)K^0_S$	yes	...	142 ± 13
$B^0 \to \eta' K^0_S$	yes	...	37 ± 16
$B^0 \to a_1^{\pm}\pi^{\mp}$	no	$(39.7 \pm 3.7) \times 10^{-6}$	7.3 ± 0.7
$B^0 \to D^{*-}(\to D\pi)\pi^+$	no	$(2.57 \pm 0.10) \times 10^{-3}$	43.8 ± 2.5
$B^0 \to D^- h^+$; $B^0 \to D^-\mu^+\nu_\mu$	no	$(2.94 \pm 0.19) \times 10^{-3}$	281 ± 20
$B^0 \to D^{*-}\rho^+$	no	$(14.2 \pm 1.4) \times 10^{-3}$	34.5 ± 4.6
$B^0 \to$ {neutral generic decays}	no	not applicable	114 ± 7
$B^+ \to$ {charged generic decays}	no	not applicable	282 ± 11

the final likelihood model—those with at least two events expected after selection. These exclusive B background modes are grouped into ten different classes that gather decays with similar kinematic and topological properties: nine for neutral B decays, one of which accounts for inclusive decays, and one for inclusive charged B decays.

Table II summarizes the ten B background classes that are used in the fit. The yields of those classes that have a clear signature in the DP are allowed to float in the maximum-likelihood fit, the remainder are fixed. When the yield of a class is varied in the maximum-likelihood fit the quoted number of events corresponds to the fit results. For the other modes, the expected numbers of selected events are computed by multiplying the selection efficiencies (estimated using MC simulated decays) by the world average branching fractions [3,32], scaled to the data set luminosity (347 fb^{-1}).

V. THE MAXIMUM-LIKELIHOOD FIT

We perform an unbinned extended maximum-likelihood fit to extract the inclusive $B^0 \to K^0_S\pi^+\pi^-$ event yield and the resonant amplitudes. The fit uses the variables $m_{\rm ES}$, ΔE, the NN output, and the SDP to discriminate signal from background. The Δt measurement allows the determination of mixing-induced CP violation and provides additional continuum background rejection.

The selected on-resonance data sample is assumed to consist of signal, continuum background, and B background components. The signal likelihood consists of the sum of a correctly reconstructed (''truth-matched,'' TM) term and a misreconstructed (''self-cross-feed,'' SCF) term. Generally, the components in the fit are separated by the flavor and tagging category of the tag side B decay.

The probability density function (PDF) $\mathcal{P}_i^c$ for an event i in tagging category c is the sum of the probability densities

TABLE III. Definitions of the different variables in the likelihood function given in Eq. (26).

Variable	Definition
$N_{\rm sig}$	total number of $K^0_S\pi^+\pi^-$ signal events in the data sample
$f^c_{\rm sig}$	fraction of signal events that are tagged in category c
$\bar{f}^c_{\rm SCF}$	fraction of SCF events in tagging category c, averaged over the DP
$\mathcal{P}^c_{\text{sig-TM},i}$	product of PDFs of the discriminating variables used in tagging category c for TM events
$\mathcal{P}^c_{\text{sig-SCF},i}$	product of PDFs of the discriminating variables used in tagging category c for SCF events
$N^c_{q\bar{q}}$	number of continuum events that are tagged in category c
$q_{{\rm tag},i}$	tag flavor of the event, defined to be $+1$ for a $B^0_{\rm tag}$ and -1 for a $\bar{B}^0_{\rm tag}$
$A_{q\bar{q}}$	parametrizes possible asymmetry in continuum events
$\mathcal{P}^c_{q\bar{q},i}$	continuum PDF for tagging category c
$N^{B^0}_{\rm class}$	number of neutral B-related background classes considered in the fit, namely, nine
N_{B^+}	number of expected charged B background events
$N_{B^0 j}$	number of expected events in the neutral B background class j
$f^c_{B^+}$	fraction of charged B background events that are tagged in category c
$f^c_{B^0 j}$	fraction of neutral B background events of class j that are tagged in category c
A_{B^+}	describes a possible asymmetry in the charged B background
$\mathcal{P}^c_{B^+,i}$	B^+ background PDF for tagging category c
$\mathcal{P}^c_{B^0,ij}$	neutral B background PDF for tagging category c and class j

of all components, namely

$$\begin{aligned}\mathcal{P}_i^c \equiv & N_{\rm sig} f_{\rm sig}^c [(1-\bar{f}_{\rm SCF}^c)\mathcal{P}_{\text{sig-TM},i}^c + \bar{f}_{\rm SCF}^c \mathcal{P}_{\text{sig-SCF},i}^c] \\ & + N_{q\bar{q}}^c \frac{1}{2}(1+q_{{\rm tag},i}A_{q\bar{q}})\mathcal{P}_{q\bar{q},i}^c \\ & + N_{B^+} f_{B^+}^c \frac{1}{2}(1+q_{{\rm tag},i}A_{B^+})\mathcal{P}_{B^+,i}^c \\ & + \sum_{j=1}^{N_{\rm class}^{B^0}} N_{B^0 j} f_{B^0 j}^c \mathcal{P}_{B^0,ij}^c. \end{aligned} \quad (26)$$

The variables are defined in Table III. The PDFs $\mathcal{P}_X^c$ ($X = \{\text{sig-TM, sig-SCF, } q\bar{q}, B^+, B^0\}$) are the product of the four PDFs of the discriminating variables, $x_1 = m_{\rm ES}$, $x_2 = \Delta E$, $x_3 =$ NN output, and the triplet $x_4 = \{m', \theta', \Delta t\}$:

$$\mathcal{P}_{X,i(j)}^c \equiv \prod_{k=1}^{4} P_{X,i(j)}^c(x_k), \quad (27)$$

where i is the event index and j is a B background class. Not all the PDFs depend on the tagging category; the general notations $P_{X,i(j)}^c$ and $\mathcal{P}_{X,i(j)}^c$ are used for simplicity. Correlations between the tag and the position in the DP are absorbed in tag-flavor-dependent SDP PDFs that are used for continuum and charged B backgrounds. The parameters A_{B^+} and $A_{q\bar{q}}$ parametrize any potential asymmetry between these PDFs. The extended likelihood over all tagging categories is given by

$$\mathcal{L} \equiv \prod_{c=1}^{7} e^{-\bar{N}^c} \prod_{i}^{N^c} \mathcal{P}_i^c, \quad (28)$$

where $\bar{N}^c$ is the total number of events expected in category c.

A total of 75 parameters are varied in the fit. They include the 12 inclusive yields (signal, four B background classes, and seven continuum yields, one per tagging category), 30 parameters for the complex amplitudes from Eq. (22), and 33 parameters of the different PDFs. The latter include most of the parameters describing the continuum distributions.

A. The Δt and Dalitz plot PDFs

The SDP PDFs require as input the DP-dependent selection efficiency, $\varepsilon = \varepsilon(m', \theta')$, and SCF fraction, $f_{\rm SCF} = f_{\rm SCF}(m', \theta')$. Both quantities are taken from MC simulation. Away from the DP corners the efficiency is uniform. It decreases when approaching the corners, where one of the three particles in the final state is nearly at rest so that the acceptance requirements on the particle reconstruction become restrictive. Combinatorial backgrounds and hence SCF fractions are large in the corners of the DP due to the presence of soft tracks.

For an event i we define the time-dependent SDP PDFs

$$P_{\text{sig-TM},i}(m', \theta', \Delta t) = \varepsilon_i (1 - f_{\text{SCF},i}) |\det J_i| |\mathcal{A}^{\pm}(\Delta t)|^2, \quad (29)$$

$$P_{\text{sig-SCF},i}(m', \theta', \Delta t) = \varepsilon_i f_{\text{SCF},i} |\det J_i| |\mathcal{A}^{\pm}(\Delta t)|^2, \quad (30)$$

where $P_{\text{sig-TM},i}(m', \theta', \Delta t)$ and $P_{\text{sig-SCF},i}(m', \theta', \Delta t)$ are normalized to unity. The phase-space integration involves the expectation values $\langle \varepsilon(1 - f_{\rm SCF}) |\det J| F_k F_{k'}^* \rangle$ and $\langle \varepsilon f_{\rm SCF} |\det J| F_k F_{k'}^* \rangle$ for TM and SCF events, where the indices k, k' run over all resonances belonging to the signal model. The expectation values are model-dependent and are computed by MC integration over the SDP:

$$\begin{aligned} & \langle \varepsilon(1 - f_{\rm SCF}) |\det J| F_k F_{k'}^* \rangle \\ & = \frac{\int_0^1 \int_0^1 \varepsilon(1 - f_{\rm SCF}) |\det J| F_k F_{k'}^* dm' d\theta'}{\int_0^1 \int_0^1 \varepsilon |\det J| F_k F_{k'}^* dm' d\theta'}, \end{aligned} \quad (31)$$

and similarly for $\langle \varepsilon f_{\rm SCF} |\det J| F_k F_{k'}^* \rangle$, where all quantities in the integrands are DP-dependent.

Equation (26) invokes the phase space-averaged SCF fraction $\bar{f}_{\rm SCF} \equiv \langle f_{\rm SCF} |\det J| F_k F_{k'}^* \rangle$. The PDF normalization is decay-dynamics-dependent and is computed iteratively. We determine the average SCF fractions separately for each tagging category from MC simulation.

The width of the dominant resonances are large compared to the mass resolution for TM events (about 8 MeV/c^2 core Gaussian resolution). We therefore neglect resolution effects in the TM model. Misreconstructed events have a poor mass resolution that strongly varies across the DP. It is described in the fit by a $2\times$ 2-dimensional resolution function

$$R_{\rm SCF}(m'_r, \theta'_r, m'_t, \theta'_t), \quad (32)$$

which represents the probability to reconstruct at the coordinates (m'_r, θ'_r) an event that has the true coordinates (m'_t, θ'_t). It obeys the unitarity condition

$$\int_0^1 \int_0^1 R_{\rm SCF}(m'_r, \theta'_r, m'_t, \theta'_t) dm'_r d\theta'_r = 1, \quad (33)$$

and is convolved with the signal model. The $R_{\rm SCF}$ function is obtained from MC simulation.

We use the signal model described in Sec. II A. It contains the dynamical information and is connected with Δt via the matrix element in Eq. (22), which intervenes in the signal PDFs defined in Eq. (29) and (30). The PDFs are diluted by the effects of mistagging and the limited vertex resolution [42]. The Δt resolution function for signal (both TM and SCF) and B background events is a sum of three Gaussian distributions. The parameters of the signal resolution function are determined by a fit to fully-reconstructed B^0 decays [40].

The charged B background contribution to the likelihood, given in Eq. (26), uses distinct SDP PDFs for each reconstructed B flavor tag, and a flavor-tag-averaged PDF

for untagged events. The PDFs are obtained from MC simulation and are described by histograms. The Δt resolution parameters are determined by a fit to fully-reconstructed B^+ decays. For the B^+ background class we adjust the effective lifetime to account for the misreconstruction of the event that modifies the nominal Δt resolution function.

The neutral B background is parametrized with PDFs that depend on the flavor tag of the event. In the case of CP eigenstates, correlations between the flavor tag and the Dalitz coordinates are expected to be small. However, non-CP eigenstates, such as $a_1^{\pm}\pi^{\mp}$, may exhibit such correlations. Both types of decays can have direct and mixing-induced CP violation. A third type of decay involves charged D mesons and does not exhibit mixing-induced CP violation, but usually has a strong correlation between the flavor tag and the DP coordinates because it consists of B-flavor eigenstates. Direct CP violation is also possible in these decays, though it is set to zero in the nominal model. The DP PDFs are obtained from MC simulation and are described by histograms. For neutral B background, the signal Δt resolution model is assumed. Note that the SDP- and Δt-dependent PDFs factorize for the charged B background modes, but not necessarily for the neutral B background due to $B^0\bar{B}^0$ mixing.

The DP treatment of the continuum events is similar to that used for charged B background. The SDP PDF for continuum background is obtained from on-resonance events selected in the $m_{\rm ES}$ sidebands and corrected for feed-through from B decays. A large number of cross checks have been performed to validate the empirical shape used. The continuum Δt distribution is parametrized as the sum of three Gaussian distributions with common mean and three distinct widths that scale with the Δt per event error. This introduces six shape parameters that are determined by the fit. The model is motivated by the observation that the mean of the Δt distribution is independent of the per event error, and that the width depends linearly on this error.

B. Description of the other variables

The $m_{\rm ES}$ distribution of TM signal events is parametrized by a bifurcated Crystal Ball function [43–45], which is a combination of a one-sided Gaussian and a Crystal Ball function. The mean and the two widths of this function are determined by the fit. The ΔE distribution of TM signal events is parametrized by a double Gaussian function. The five parameters of this function are determined by the fit. Both $m_{\rm ES}$ and ΔE PDFs are described by histograms, taken from the distributions found in appropriate MC samples, for SCF signal events and all B background classes. Exceptions to this are the $m_{\rm ES}$ PDFs for the $B^0 \to D^-\pi^+$ and $B^0 \to J/\psi K_S^0$ components, and the ΔE PDF for $B^0 \to D^-\pi^+$, which are the same as the corresponding distributions of TM signal events. The $m_{\rm ES}$ and ΔE PDFs for continuum events are parametrized by an ARGUS shape function [46] and a first-order polynomial, respectively, with parameters determined by the fit.

We use histograms to empirically describe the distributions of the NN output found in the MC simulation for TM and SCF signal events and for all B background classes. We distinguish tagging categories for TM signal events to account for differences observed in the shapes. The continuum NN distribution is parametrized by a third-order polynomial that is constrained to take positive values in the range populated by the data. The coefficients of the polynomial are determined by the fit. Continuum events exhibit a correlation between the DP coordinates and the shape of the event that is exploited in the NN. To correct for this effect, we introduce a linear dependence of the polynomial coefficients on the variable $\Delta_{\rm DP}$, defined as the smallest of the three invariant masses, and is thus a measure of the distance of the DP coordinates from the kinematic boundaries of the DP. The parameters describing this dependence are determined by the fit.

VI. RESULTS

The standard and square Dalitz plots of the selected data sample are shown in Fig. 1. The maximum-likelihood fit of 22 525 candidates results in a $B^0 \to K_S^0\pi^+\pi^-$ event yield of 2182 ± 64 and a continuum yield of 14240 ± 126, where the uncertainties are statistical only. The remaining number of events is covered by the yields of backgrounds from charged and neutral B decays, where the dominant contributions are 3361 ± 60 $B^0 \to D^-\pi^+$ and 1804 ± 44 $B^0 \to J/\psi K_S^0$ events.

When the fit is repeated starting from input parameter values randomly chosen within wide ranges above and below the nominal values for the magnitudes and within the [0–360°] interval for the phases, we observe convergence toward two solutions with minimum values of the negative log likelihood function $-2\log\mathcal{L}$ that are equal within 0.32 units. In the following, we refer to them as solution I (the global minimum) and solution II (a local minimum). No other local minima were found. Between the two solutions, the fit values for most free parameters are very similar. Exceptions occur among isobar parameters, and most particularly isobar phases, some of which can differ significantly. A possible interpretation of the double solution as a result of the trigonometric ambiguity in the $f_0(980)K_S^0$ resonant mode is discussed below. However, the significance with which one of the solutions is preferred is expected to increase with statistics.

For a given event i, we define the likelihood ratio as $R \equiv \mathcal{P}_{\text{sig-TM},i}/\mathcal{P}_i$ (see Eq. (26) and explanations below). Figure 2 shows distributions of $\log R$ for all the events entering the fit, and for the signal-like region. We obtain signal enriched samples that are used in some of the figures below, by removing events with small values of R; in each case R is computed excluding the variable being plotted.

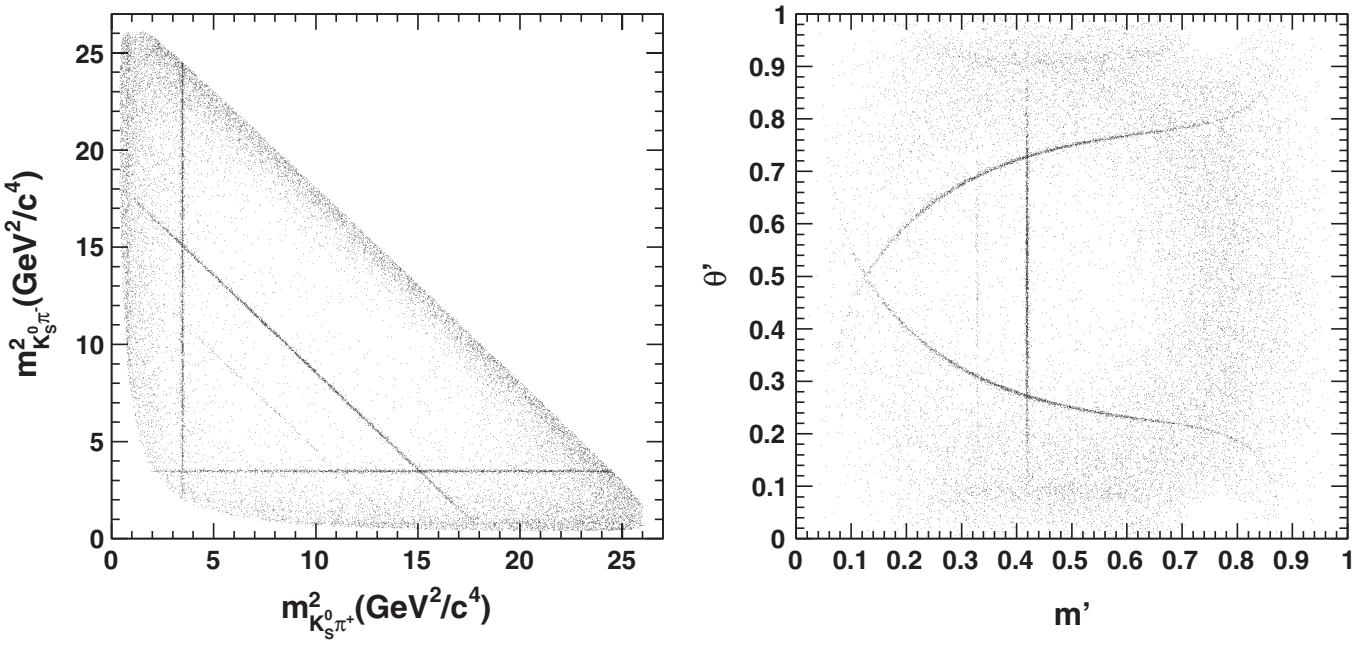

FIG. 1. Standard (left) and square (right) Dalitz plots of the selected data sample of 22 525 $B \to K^0_S\pi^+\pi^-$ candidates. The narrow bands correspond to $D^{\mp}\pi^{\pm}$, $J/\psi K^0_S$, and $\psi(2S)K^0_S$ background events.

Figure 3 shows distributions of ΔE, $m_{\rm ES}$, and the NN output which are enhanced in signal content by requirements on R. Figures 4–7 show similar distributions for $m(\pi^+\pi^-)$, $m(K^0_s\pi)$, and $\Delta_{\rm DP}$. These distributions illustrate the good quality of the fit in the signal-enhanced regions. Signal enriched distributions of Δt and Δt asymmetry for events in the regions of $f_0(980)K^0_S$ and $\rho^0(770)K^0_S$ are shown in Fig. 8.

In the fit, we measure directly the relative magnitudes and phases of the different components of the signal model. The magnitude and phase of the $B^0 \to f_0(980)K^0_S$ amplitude are fixed to 4 and 0, respectively, as a reference. The results corresponding to the two solutions are given together with their statistical uncertainties in Table IV. The full (statistical, systematic, and model-dependent) correlation matrices between the magnitudes and the phases for

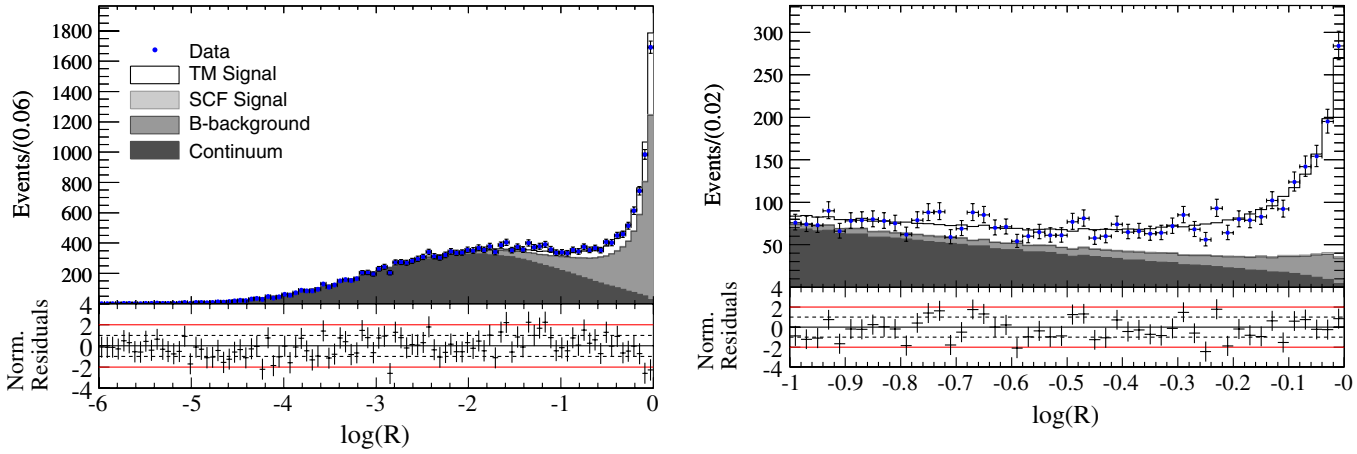

FIG. 2 (color online). Distributions of the logarithm of likelihood ratio ($\log R$) for all events entering the fit (left) and in the signal-like region (right). In the right-hand side plot, a veto in the $D^-\pi^+$, $J/\psi K^0_S$, and $\psi(2S)K^0_S$ bands has been applied. Points with error bars give the on-resonance data. The solid histogram shows the projection of the fit result. The dark, medium, and light shaded areas represent, respectively, the contribution from continuum events, the sum of continuum events and the B background expectation, and the sum of these and the misreconstructed signal events. The last contribution is hardly visible due to its small fraction. Below each bin are shown the residuals, normalized in error units. The parallel dotted and full lines mark the one and two standard deviation levels, respectively. Points, histograms, shaded areas, and residual plots have similar definitions in Figs. 3 to 8.

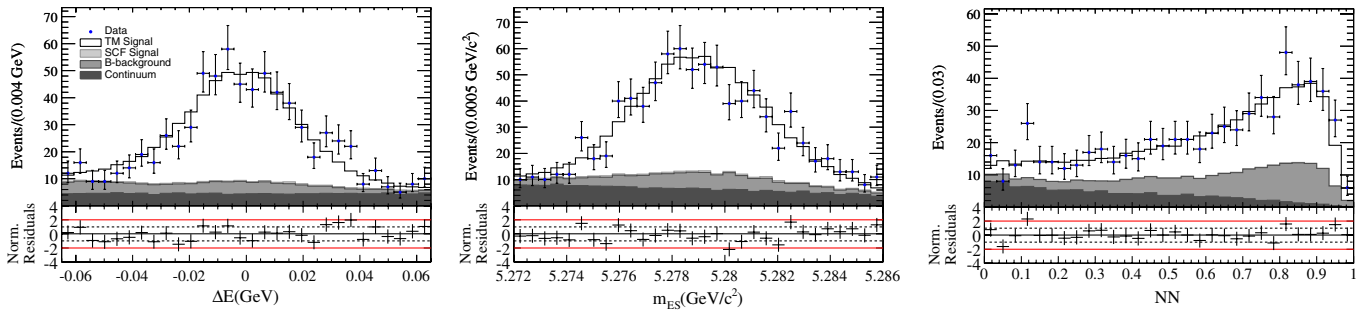

FIG. 3 (color online). Distributions of ΔE (left), $m_{\rm ES}$ (center), and NN output (right) for a sample enhanced in $B^0 \to K^0_S \pi^+ \pi^-$ signal with a requirement on the likelihood ratio R computed without the variable being plotted. In each case the applied cut rejects 99% of continuum background, while retaining 28% of signal for ΔE and $m_{\rm ES}$, and 16% for NN. A veto in the $D^- \pi^+$ and $J/\psi K^0_S$ bands has been applied.

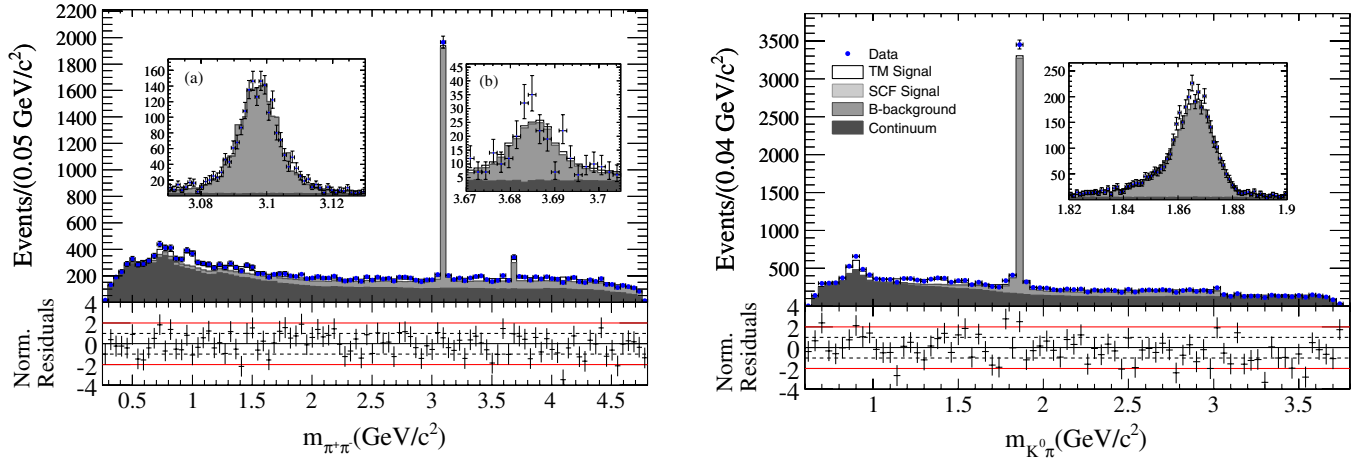

FIG. 4 (color online). Spectra of $m_{\pi^+\pi^-}$ (left) and symmetrized $m_{K^0_S\pi}$ (right) for the whole data sample. For $m_{\pi^+\pi^-}$, the insets show the J/ψ region (a) and in the $\psi(2S)$ region (b). The symmetrized $m_{K^0_S\pi}$ is obtained by folding the SDP with respect to the θ' variable at 0.5. The inset shows the D region.

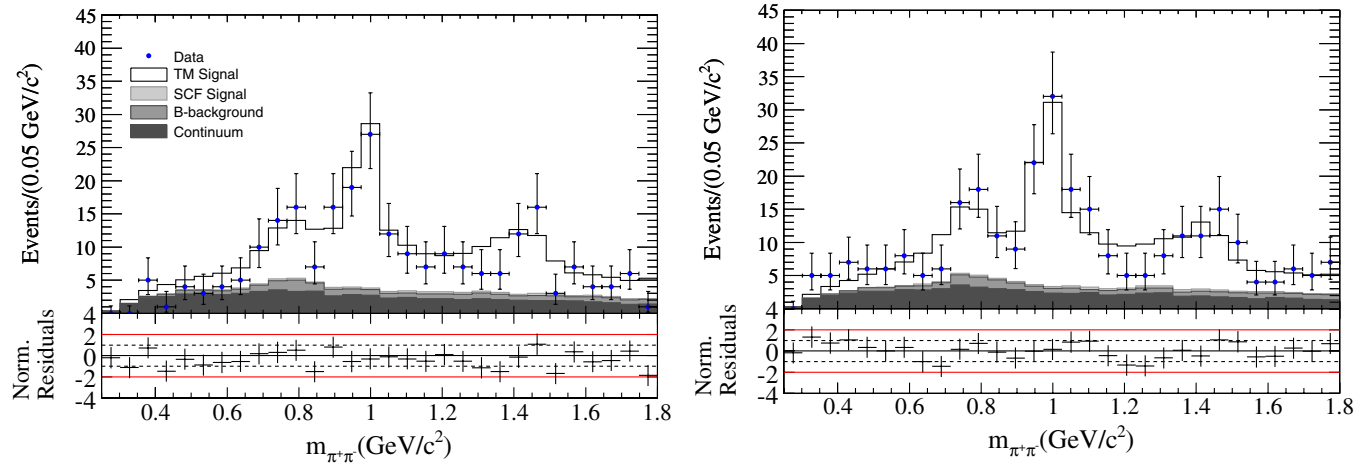

FIG. 5 (color online). Distribution of $m_{\pi^+\pi^-}$ for a sample enhanced in $B^0 \to K^0_S \pi^+ \pi^-$ signal, showing the $f_0(980)K^0_S$ and $\rho^0(770)K^0_S$ signal region for positive (left) and negative (right) $\pi^+\pi^-$ helicity. The contribution from $f_X(1300)K^0_S$ and $f_2(1270)K^0_S$ are also visible. A veto in the $D\pi$ band has been applied. The Δt and DP PDFs have been excluded from the likelihood ratio R used to enhance the sample in signal events. The cut on R retains 21% of signal, while rejecting 99% of continuum.

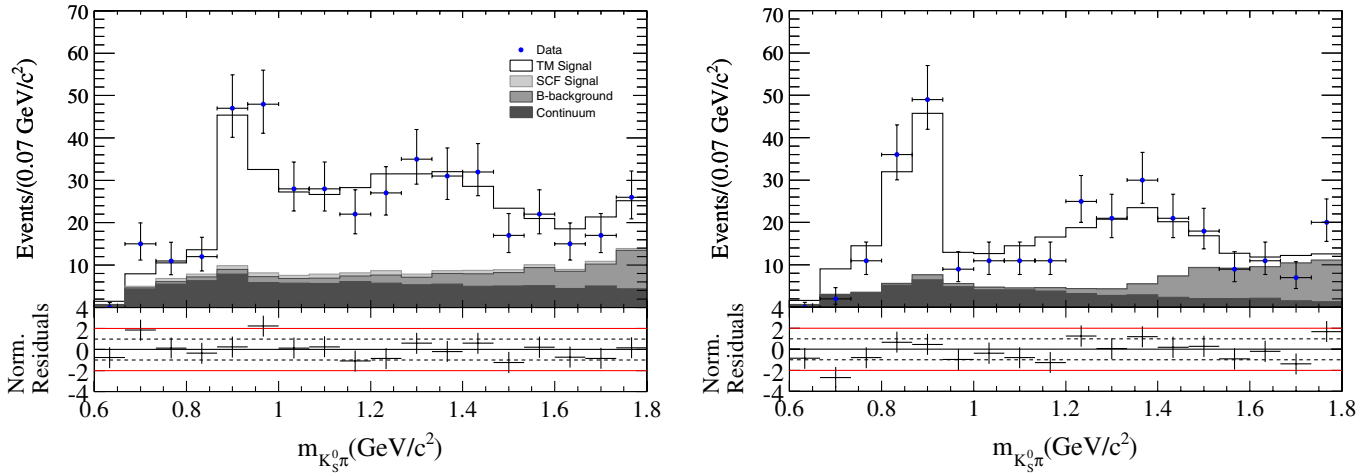

FIG. 6 (color online). Distributions of $m_{K^0_S\pi}$ for a sample enhanced in $B^0 \to K^0_S\pi^+\pi^-$ signal, showing the $K^*(892)\pi$ and $K^*(1430)\pi$ signal region for positive (left) and negative (right) $K^0_S\pi$ helicity. A veto in the $J/\psi K^0_S$ and $\psi(2S)K^0_S$ bands has been applied. The Δt and DP PDFs have been excluded from the definition of the likelihood ratio used to enhance the sample in signal events. The cut on R retains 18% of signal while rejecting 94% of continuum. An interference between the vector and scalar K^{*+} is apparent through a positive (negative) forward-backward asymmetry below (above) the $K^*(892)$.

the two solutions are given in the appendix. The measured relative amplitudes c_k, where the index represents an intermediate resonance, are used to extract the Q2B parameters defined below.

For a resonant decay mode k which is a CP eigenstate, the following Q2B parameters are extracted: the angle $\beta_{\rm eff}$ defined as

$$\beta_{\rm eff}(k) = \tfrac{1}{2}\arg(c_k\bar{c}^*_k) \tag{34}$$

and the direct and mixing-induced CP asymmetries, defined as

$$C(k) = \frac{|c_k|^2 - |\bar{c}_k|^2}{|c_k|^2 + |\bar{c}_k|^2}, \tag{35}$$

$$S(k) = \frac{2\,\mathrm{Im}(\bar{c}_k c^*_k)}{|c_k|^2 + |\bar{c}_k|^2}. \tag{36}$$

For a flavor-specific resonant decay mode k such as $B^0 \to K^{*+}(892)\pi^-$, it is customary to define the direct CP asymmetry parameter A_{CP} as

$$A_{CP}(k) = \frac{|\bar{c}_{\bar{k}}|^2 - |c_k|^2}{|\bar{c}_{\bar{k}}|^2 + |c_k|^2}. \tag{37}$$

For a pair of resonances k and k', the phase $\phi(k, k')$ relating their amplitudes c_k and $c_{k'}$, defined as

$$\phi(k, k') = \arg(c_k c^*_{k'}), \tag{38}$$

can be accessed by exploiting the interference pattern in the DP areas where k and k' overlap; correspondingly, the phase $\bar{\phi}(k, k')$ for the CP-conjugated amplitudes $\bar{c}_k$ and $\bar{c}_{k'}$ is

$$\bar{\phi}(k, k') = \arg(\bar{c}_k \bar{c}^*_{k'}). \tag{39}$$

From these two phases, the difference $\Delta\phi(k, k') = \bar{\phi}(k, k') - \phi(k, k')$, can be extracted. This parameter is a direct CP violation observable, and can only be accessed in an amplitude analysis.

For a resonant decay mode k, the phase relating its amplitude c_k to its charge conjugate $\bar{c}_k$ is defined as

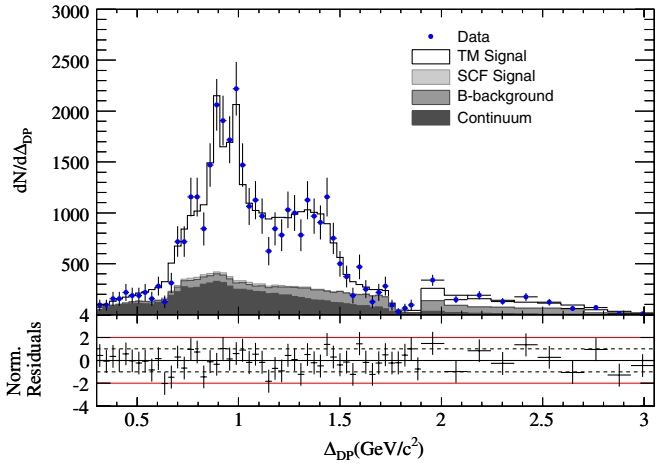

FIG. 7 (color online). Distributions of the $\Delta_{\rm DP}$ variable, for a sample enhanced in $B^0 \to K^0_S\pi^+\pi^-$ signal. The $\Delta_{\rm DP}$ variable is defined as $\min(m_{K^0_S\pi^+}, m_{K^0_S\pi^-}, m_{\pi^+\pi^-})$. Small (large) values of $\Delta_{\rm DP}$ correspond to the edges (center) of the DP. On the left (right) side of the figure, for $\Delta_{\rm DP} < 1.9$ GeV/c^2 (> 1.9 GeV/c^2), the dominant contribution to the signal is from the light resonances (the NR) component of the signal model. A veto in the $D\pi$, $J/\psi K^0_S$, and $\psi(2S)K^0_S$ bands has been applied. The Δt and DP PDFs have been excluded from the likelihood ratio R used to enhance the sample in signal events. The cut on R retains 37% of signal while rejecting 88% of continuum.

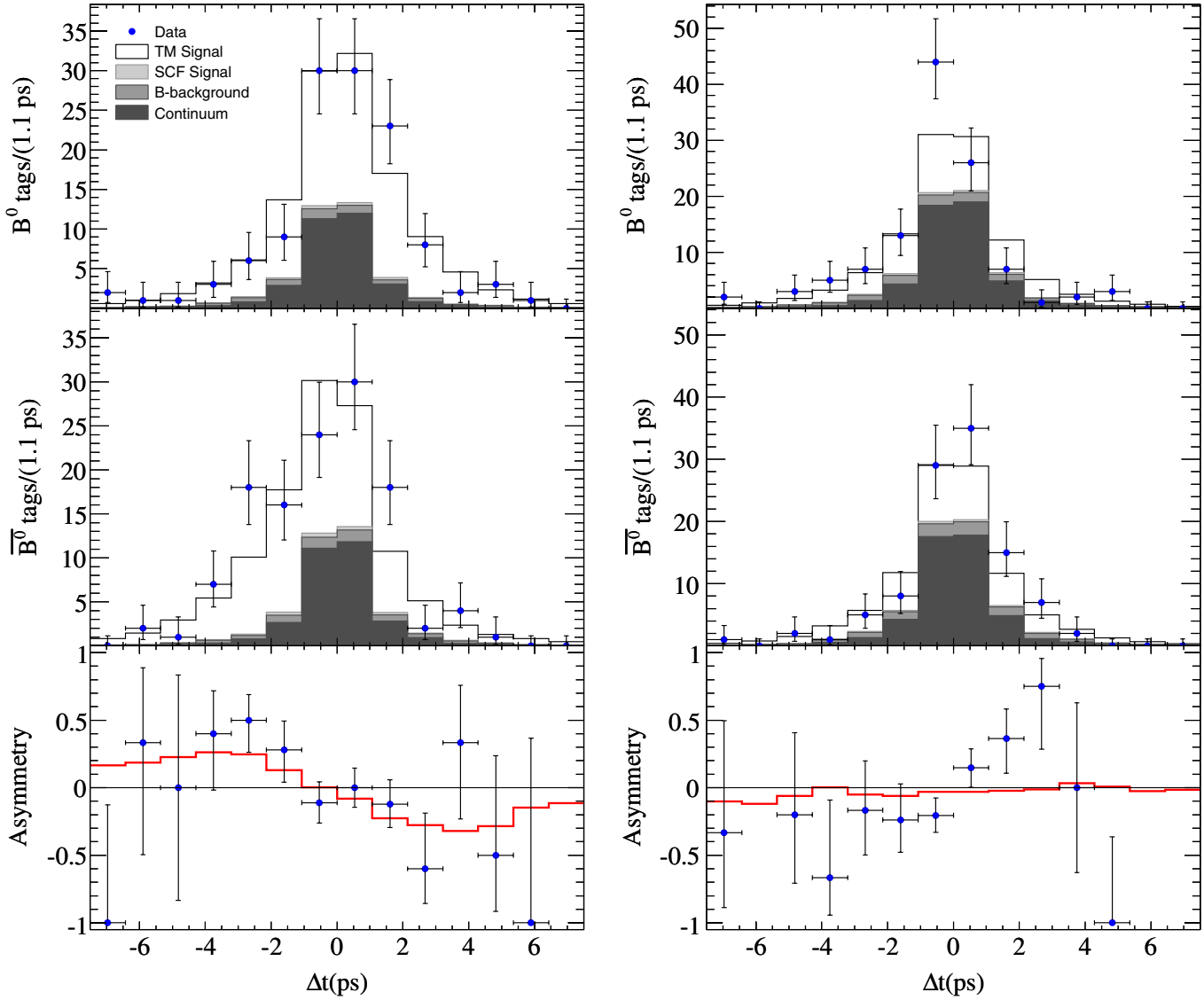

FIG. 8 (color online). Distributions of Δt when the $B^0_{\rm tag}$ is a B^0 (top), $\bar{B}^0$ (middle), and the derived Δt asymmetry (bottom). Plots on the left (right) hand side, correspond to events in the $f_0(980)K^0_S$ ($\rho^0(770)K^0_S$) region. These distributions correspond to samples where the $D^-\pi^+$ and $J/\psi K^0_S$ bands are removed from the DP, and the Δt and DP PDFs have been excluded from the likelihood ratio R used to enhance the sample in signal events. The cut on R retains 24% of signal while rejecting 98% of continuum.

$$\Delta\Phi(k) = \arg(c_k \bar{c}^*_k); \tag{40}$$

here it is worth recalling that we use a convention in which the $\bar{B}^0$ decay amplitudes have absorbed the phase from $B^0\bar{B}^0$ mixing, and so the phase of q/p is implicit in the $\Delta\Phi(k)$ parameter. Although the definition of this parameter is technically similar to the $\beta_{\rm eff}$ phase defined in Eq. (34), they differ in their physical interpretation. The parameter $\beta_{\rm eff}$ quantifies the time-dependent mixing-induced CP asymmetry, and therefore is most relevant for the CP eigenstate modes, such as $\rho^0(770)K^0_S$ and $f_0(980)K^0_S$. On the other hand the $\Delta\Phi(k)$ parameter concerns mostly flavor-specific modes, such as $B^0 \to K^{*+}(892)\pi^-$, for which there is no interference between decays with and without mixing. For such modes, sensitivity to $\Delta\Phi(k)$ is provided indirectly by the interference pattern of the resonance k with other modes that are accessible both to B^0 and $\bar{B}^0$ decays.

We also extract the relative fit fraction FF of a Q2B channel k, which is calculated as

$$FF(k) = \frac{(|c_k|^2 + |\bar{c}_k|^2)\langle F_k F^*_k\rangle}{\sum_{\mu\nu}(c_\mu c^*_\nu + \bar{c}_\mu \bar{c}^*_\nu)\langle F_\mu F^*_\nu\rangle}, \tag{41}$$

where the terms

$$\langle F_\mu F^*_\nu\rangle = \iint F_\mu F^*_\nu ds_+ ds_- \tag{42}$$

are obtained by integration over the complete Dalitz plot.

TABLE IV. Results of fit to data for the isobar amplitudes with statistical uncertainties. Both solutions are shown.

Isobar Amplitude	Solution I Magnitude	Solution I Phase (°)	Solution II Magnitude	Solution II Phase (°)
$c_{f_0(980)K^0_S}$	4.0	0.0	4.0	0.0
$\bar{c}_{f_0(980)K^0_S}$	3.7 ± 0.4	-73.9 ± 19.6	3.2 ± 0.6	-112.3 ± 20.9
$c_{\rho(770)K^0_S}$	0.10 ± 0.02	35.6 ± 14.9	0.09 ± 0.02	66.7 ± 18.3
$\bar{c}_{\rho(770)K^0_S}$	0.11 ± 0.02	15.3 ± 20.0	0.10 ± 0.03	-0.1 ± 18.2
$c_{K^{*+}(892)\pi^-}$	0.154 ± 0.016	-138.7 ± 25.7	0.145 ± 0.017	-107.0 ± 24.1
$\bar{c}_{K^{*-}(892)\pi^+}$	0.125 ± 0.015	163.1 ± 23.0	0.119 ± 0.015	76.4 ± 23.0
$c_{(K\pi)^{*+}_0\pi^-}$	6.9 ± 0.6	-151.7 ± 19.7	6.5 ± 0.6	-122.5 ± 20.3
$\bar{c}_{(K\pi)^{*-}_0\pi^+}$	7.6 ± 0.6	136.2 ± 19.8	7.3 ± 0.7	52.6 ± 20.3
$c_{f_2(1270)K^0_S}$	0.014 ± 0.002	5.8 ± 19.2	0.012 ± 0.003	23.9 ± 22.7
$\bar{c}_{f_2(1270)K^0_S}$	0.011 ± 0.003	-24.0 ± 28.0	0.011 ± 0.003	-83.3 ± 24.3
$c_{f_X(1300)K^0_S}$	1.41 ± 0.23	43.2 ± 22.0	1.40 ± 0.28	85.9 ± 24.8
$\bar{c}_{f_X(1300)K^0_S}$	1.24 ± 0.27	31.6 ± 23.0	1.02 ± 0.33	-67.9 ± 22.1
c_{NR}	2.6 ± 0.5	35.3 ± 16.4	1.9 ± 0.7	56.7 ± 23.6
$\bar{c}_{NR}$	2.7 ± 0.6	36.1 ± 18.3	3.1 ± 0.6	-45.2 ± 17.8
$c_{\chi_{c0}K^0_S}$	0.33 ± 0.15	61.4 ± 44.5	0.28 ± 0.16	51.9 ± 38.4
$\bar{c}_{\chi_{c0}K^0_S}$	0.44 ± 0.09	15.1 ± 30.0	0.43 ± 0.08	-58.5 ± 27.9

The total fit fraction is defined as the algebraic sum of all fit fractions. This quantity is not necessarily unity due to the potential presence of net constructive or destructive interference. Using the relative fit fractions, we calculate the branching fraction $\mathcal{B}$ for the intermediate mode k as

$$FF(k) \times \mathcal{B}(B^0 \to K^0_S\pi^+\pi^-), \tag{43}$$

where $\mathcal{B}(B^0 \to K^0_S\pi^+\pi^-)$ is the total inclusive branching fraction

$$\mathcal{B}(B^0 \to K^0_S\pi^+\pi^-) = \frac{N_{\rm sig}}{\bar{\varepsilon}N_{B\bar{B}}}. \tag{44}$$

We compute the average efficiency, $\bar{\varepsilon}$, by weighting MC events with the measured intensity distribution of signal events, $(|\mathcal{A}(\mathrm{DP})|^2 + |\bar{\mathcal{A}}(\mathrm{DP})|^2)/2$. The term $N_{B\bar{B}}$ is the total number of $B\bar{B}$ pairs in the sample. Finally, we use the following integrals of amplitudes over the complete Dalitz plot to measure the inclusive direct CP-asymmetry:

$$A^{\rm incl}_{CP} = \frac{\int\int(|\bar{\mathcal{A}}|^2 - |\mathcal{A}|^2)ds_+ds_-}{\int\int(|\bar{\mathcal{A}}|^2 + |\mathcal{A}|^2)ds_+ds_-}. \tag{45}$$

The Q2B parameters and fit fractions are given in Table V, together with their statistical and systematic errors. The branching fractions are shown in Table VI.

To extract the statistical uncertainties on the Q2B parameters we perform likelihood scans, not relying on any assumption about the shape of the likelihood function. Since the Q2B parameters are not directly used in the fit, we instead must perform the scan fixing one or two parameters among the signal model magnitudes and phases. These are chosen in such a way that the resulting likelihood curve can be trivially interpreted in terms of the Q2B parameter of interest. In each case the chosen parameters are fixed at several consecutive values, for each of which the fit to the data is repeated. The error on the Q2B parameter is determined by the points, or the contour, where the $-2\log\mathcal{L}$ function changes by one unit with respect to its minimum value. Systematic uncertainties are discussed in Sec. VII. Results of the likelihood scans in terms of $-2\Delta\log\mathcal{L}$ are shown in Figs. 9–16.

The measurements of time-dependent CP-violation in the $f_0(980)K^0_S$ and $\rho^0(770)K^0_S$ modes are presented as two-dimensional likelihood scans in the $(\beta_{\rm eff}, C)$ plane, shown in Fig. 9. The scans are displayed as confidence level contours after two-dimensional convolution with the covariance matrix of systematic uncertainties. In the same figure, one-dimensional likelihood scans of $\beta_{\rm eff}$ are also displayed. For $f_0(980)K^0_S$ the two solutions lie below and above 45 degrees and correspond very closely to the trigonometric ambiguity between a given value of $\beta_{\rm eff}$ and $90° - \beta_{\rm eff}$ (mirror solutions). On the other hand, for $\rho^0(770)K^0_S$ both solutions are below 45 degrees. In this case the trigonometric ambiguities of the two observed solutions are suppressed at 3.6 and 2.0 standard deviations (σ), respectively.

The $(\beta_{\rm eff}, C)$ plane can be transformed to the more familiar (S, C) plane using Eq. (34)–(36). The corresponding two-dimensional contours are shown in Fig. 10. While a part of the information on the phases is lost, this repre-

TABLE V. Summary of measurements of the Q2B parameters for solutions I and II. The first uncertainty is statistical, the second is systematic, and the third represents the DP signal model dependence. We also show the total (statistical and systematic) linear correlations between the parameters $\beta_{\rm eff}$ (S) and C. Phases are given in degrees and FFs in percent.

Parameter	Solution I	Solution II
$C(f_0(980)K^0_S)$	$0.08 \pm 0.19 \pm 0.03 \pm 0.04$	$0.23 \pm 0.19 \pm 0.03 \pm 0.04$
$\beta_{\rm eff}(f_0(980)K^0_S)$	$36.0 \pm 9.8 \pm 2.1 \pm 2.1$	$56.2 \pm 10.4 \pm 2.1 \pm 2.1$
$S(f_0(980)K^0_S)$	$-0.96^{+0.21}_{-0.04} \pm 0.03 \pm 0.02$	$-0.90^{+0.26}_{-0.08} \pm 0.03 \pm 0.02$
Corr$[\beta_{\rm eff}(f_0(980)K^0_S), C(f_0(980)K^0_S)]$	-3.1%	-17.0%
Corr$[S(f_0(980)K^0_S), C(f_0(980)K^0_S)]$	19.7%	12.5%
$FF(f_0(980)K^0_S)$	$13.8^{+1.5}_{-1.4} \pm 0.8 \pm 0.6$	$13.5^{+1.4}_{-1.3} \pm 0.8 \pm 0.6$
$C(\rho^0(770)K^0_S)$	$-0.05 \pm 0.26 \pm 0.10 \pm 0.03$	$-0.14 \pm 0.26 \pm 0.10 \pm 0.03$
$\beta_{\rm eff}(\rho^0(770)K^0_S)$	$10.2 \pm 8.9 \pm 3.0 \pm 1.9$	$33.4 \pm 10.4 \pm 3.0 \pm 1.9$
$S(\rho^0(770)K^0_S)$	$0.35^{+0.26}_{-0.31} \pm 0.06 \pm 0.03$	$0.91^{+0.07}_{-0.19} \pm 0.06 \pm 0.03$
Corr$[\beta_{\rm eff}(\rho^0(770)K^0_S), C(\rho^0(770)K^0_S)]$	-23.0%	-34.0%
Corr$[S(\rho^0(770)K^0_S), C(\rho^0(770)K^0_S)]$	-21.3%	-10.4%
$FF(\rho^0(770)K^0_S)$	$8.6^{+1.4}_{-1.3} \pm 0.5 \pm 0.2$	$8.5^{+1.3}_{-1.2} \pm 0.5 \pm 0.2$
$A_{CP}(K^*(892)\pi)$	$-0.21 \pm 0.10 \pm 0.01 \pm 0.02$	$-0.19^{+0.10}_{-0.11} \pm 0.01 \pm 0.02$
$\Delta\Phi(K^*(892)\pi)$	$58.3 \pm 32.7 \pm 4.6 \pm 8.1$	$176.6 \pm 28.8 \pm 4.6 \pm 8.1$
$FF(K^*(892)\pi)$	$11.0^{+1.2}_{-1.0} \pm 0.6 \pm 0.8$	$10.9^{+1.2}_{-1.0} \pm 0.6 \pm 0.8$
$A_{CP}((K\pi)^*_0\pi)$	$0.09 \pm 0.07 \pm 0.02 \pm 0.02$	$0.12^{+0.07}_{-0.06} \pm 0.02 \pm 0.02$
$\Delta\Phi((K\pi)^*_0\pi)$	$72.2 \pm 24.6 \pm 4.1 \pm 4.4$	$-175.1 \pm 22.6 \pm 4.1 \pm 4.4$
$FF((K\pi)^*_0\pi)$	$45.2 \pm 2.3 \pm 1.9 \pm 0.9$	$46.1 \pm 2.4 \pm 1.9 \pm 0.9$
$C(f_2(1270)K^0_S)$	$0.28^{+0.35}_{-0.40} \pm 0.08 \pm 0.07$	$0.09 \pm 0.46 \pm 0.08 \pm 0.07$
$\beta_{\rm eff}(f_2(1270)K^0_S)$	$14.9 \pm 17.9 \pm 3.1 \pm 5.2$	$53.6 \pm 16.7 \pm 3.1 \pm 5.2$
$S(f_2(1270)K^0_S)$	$-0.48 \pm 0.52 \pm 0.06 \pm 0.10$	$-0.95 \pm 0.17 \pm 0.06 \pm 0.10$
Corr$[\beta_{\rm eff}(f_2(1270)K^0_S), C(f_2(1270)K^0_S)]$	11.5%	-2.8%
Corr$[S(f_2(1270)K^0_S), C(f_2(1270)K^0_S)]$	0.9%	21.2%
$FF(f_2(1270)K^0_S)$	$2.3^{+0.8}_{-0.7} \pm 0.2 \pm 0.7$	$2.3^{+0.9}_{-0.7} \pm 0.2 \pm 0.7$
$C(f_X(1300)K^0_S)$	$0.13^{+0.33}_{-0.35} \pm 0.04 \pm 0.09$	$0.30^{+0.34}_{-0.41} \pm 0.04 \pm 0.09$
$\beta_{\rm eff}(f_X(1300)K^0_S)$	$5.8 \pm 15.2 \pm 2.2 \pm 2.3$	$76.9 \pm 13.8 \pm 2.2 \pm 2.3$
$S(f_X(1300)K^0_S)$	$-0.20 \pm 0.52 \pm 0.07 \pm 0.07$	$-0.42 \pm 0.41 \pm 0.07 \pm 0.07$
Corr$[\beta_{\rm eff}(f_X(1300)K^0_S), C(f_X(1300)K^0_S)]$	-27.0%	-9.3%
Corr$[S(f_X(1300)K^0_S), C(f_X(1300)K^0_S)]$	28.5%	6.1%
$FF(f_X(1300)K^0_S)$	$3.6^{+1.0}_{-0.9} \pm 0.3 \pm 0.9$	$3.5^{+1.0}_{-0.8} \pm 0.3 \pm 0.9$
$C(NR)$	$0.01 \pm 0.25 \pm 0.06 \pm 0.05$	$-0.45^{+0.28}_{-0.24} \pm 0.06 \pm 0.05$
$\beta_{\rm eff}(NR)$	$0.4 \pm 8.8 \pm 1.9 \pm 3.8$	$51.0 \pm 13.3 \pm 1.9 \pm 3.8$
$S(NR)$	$-0.01 \pm 0.31 \pm 0.05 \pm 0.09$	$-0.87 \pm 0.18 \pm 0.05 \pm 0.09$
Corr$[\beta_{\rm eff}(NR), C(NR)]$	-10.6%	-37.9%
Corr$[S(NR), C(NR)]$	10.6%	-91.5%
$FF(NR)$	$11.5 \pm 2.0 \pm 1.0 \pm 0.6$	$12.6 \pm 2.0 \pm 1.0 \pm 0.6$
$C(\chi_{c0}K^0_S)$	$-0.29^{+0.53}_{-0.44} \pm 0.03 \pm 0.05$	$-0.41^{+0.54}_{-0.42} \pm 0.03 \pm 0.05$
$\beta_{\rm eff}(\chi_{c0}K^0_S)$	$23.2 \pm 22.4 \pm 2.3 \pm 4.2$	$55.2 \pm 23.3 \pm 2.3 \pm 4.2$
$S(\chi_{c0}K^0_S)$	$-0.69 \pm 0.52 \pm 0.04 \pm 0.07$	$-0.85 \pm 0.34 \pm 0.04 \pm 0.07$
Corr$[\beta_{\rm eff}(\chi_{c0}K^0_S), C(\chi_{c0}K^0_S)]$	-5.8%	-5.8%
Corr$[S(\chi_{c0}K^0_S), C(\chi_{c0}K^0_S)]$	-19.1%	-74.2%
$FF(\chi_{c0}K^0_S)$	$1.04^{+0.41}_{-0.33} \pm 0.04 \pm 0.11$	$0.99^{+0.37}_{-0.30} \pm 0.04 \pm 0.11$
total FF	$97.2^{+1.7}_{-1.3} \pm 2.1 \pm 1.15$	$98.3^{+1.5}_{-1.3} \pm 2.1 \pm 1.15$
$A^{\rm incl}_{CP}$	$-0.01 \pm 0.05 \pm 0.01 \pm 0.01$	$0.01 \pm 0.05 \pm 0.01 \pm 0.01$
$\phi(f^0(980)K^0_S, \rho(770)K^0_S)$	$-35.6 \pm 14.9 \pm 6.1 \pm 4.4$	$-66.7 \pm 18.3 \pm 6.1 \pm 4.4$
$\phi(K^*(892)\pi, (K\pi)^*_0\pi)$	$13.0 \pm 10.9 \pm 4.6 \pm 4.7$	$15.5 \pm 10.2 \pm 4.6 \pm 4.7$
$\phi(\rho(770)K^0_S, K^*(892)\pi)$	$174.3 \pm 28.0 \pm 8.7 \pm 12.7$	$-173.7 \pm 29.8 \pm 8.7 \pm 12.7$
$\phi(\rho(770)K^0_S, (K\pi)^*_0\pi)$	$-172.8 \pm 22.6 \pm 10.1 \pm 8.7$	$-170.8 \pm 26.8 \pm 10.1 \pm 8.7$
$\bar{\phi}(f^0(980)K^0_S, \rho(770)K^0_S)$	$-89.2 \pm 17.1 \pm 8.5 \pm 7.2$	$-112.2 \pm 17.8 \pm 8.5 \pm 7.2$
$\bar{\phi}(K^*(892)\pi, (K\pi)^*_0\pi)$	$26.9 \pm 9.2 \pm 4.9 \pm 6.1$	$23.8 \pm 9.1 \pm 4.9 \pm 6.1$
$\bar{\phi}(\rho(770)K^0_S, K^*(892)\pi)$	$-147.8 \pm 24.7 \pm 11.3 \pm 11.9$	$-76.5 \pm 24.0 \pm 11.3 \pm 11.9$
$\bar{\phi}(\rho(770)K^0_S, (K\pi)^*_0\pi)$	$-120.9 \pm 21.6 \pm 8.7 \pm 7.3$	$-52.7 \pm 21.4 \pm 8.7 \pm 7.3$

TABLE VI. Summary of measurements of branching fractions averaged over charge conjugate states. The quoted numbers are obtained by multiplying the corresponding fit fractions by the measured inclusive $B^0 \to K^0\pi^-\pi^-$ branching fraction. R denotes an intermediate resonant state and h stands for a final state hadron: a charged pion or a K^0. To correct for the secondary branching fractions we use the values from Ref. [32] and $\mathcal{B}(K^{*+}(892) \to K^0\pi^+) = \frac{2}{3}$. The first uncertainty is statistical, the second is systematic, and the third represents the DP signal model dependence. The fourth errors, when applicable, are due to the uncertainties on the secondary branching fractions. The quoted central values correspond to the global minimum, and errors account for the presence of the second solution.

Mode	$\mathcal{B}(B^0 \to \text{Mode}) \times \mathcal{B}(R \to hh) \times 10^{-6}$	$\mathcal{B}(B^0 \to \text{Mode}) \times 10^{-6}$
Inclusive $B^0 \to K^0\pi^+\pi^-$	...	$50.15 \pm 1.47 \pm 1.60 \pm 0.73$
$f_0(980)K^0$	$6.92 \pm 0.77 \pm 0.46 \pm 0.32$	...
$\rho^0(770)K^0$	$4.31^{+0.70}_{-0.61} \pm 0.29 \pm 0.12$	$4.36^{+0.71}_{-0.62} \pm 0.29 \pm 0.12 \pm 0.01$
$K^{*+}(892)\pi^-$	$5.52^{+0.61}_{-0.54} \pm 0.35 \pm 0.41$	$8.29^{+0.92}_{-0.81} \pm 0.53 \pm 0.62$
$(K\pi)^{*+}_0\pi^-$	$22.7^{+1.7}_{-1.3} \pm 1.2 \pm 0.6$	...
$f_2(1270)K^0$	$1.15^{+0.42}_{-0.35} \pm 0.11 \pm 0.35$	$2.71^{+0.99}_{-0.83} \pm 0.26 \pm 0.83^{+0.08}_{-0.04}$
$f_X(1300)K^0$	$1.81^{+0.55}_{-0.45} \pm 0.16 \pm 0.45$	...
flat NR	...	$5.77^{+1.61}_{-1.00} \pm 0.53 \pm 0.31$
$\chi_{c0}K^0$	$0.52^{+0.20}_{-0.16} \pm 0.03 \pm 0.06$	$142^{+55}_{-44} \pm 8 \pm 16 \pm 12$

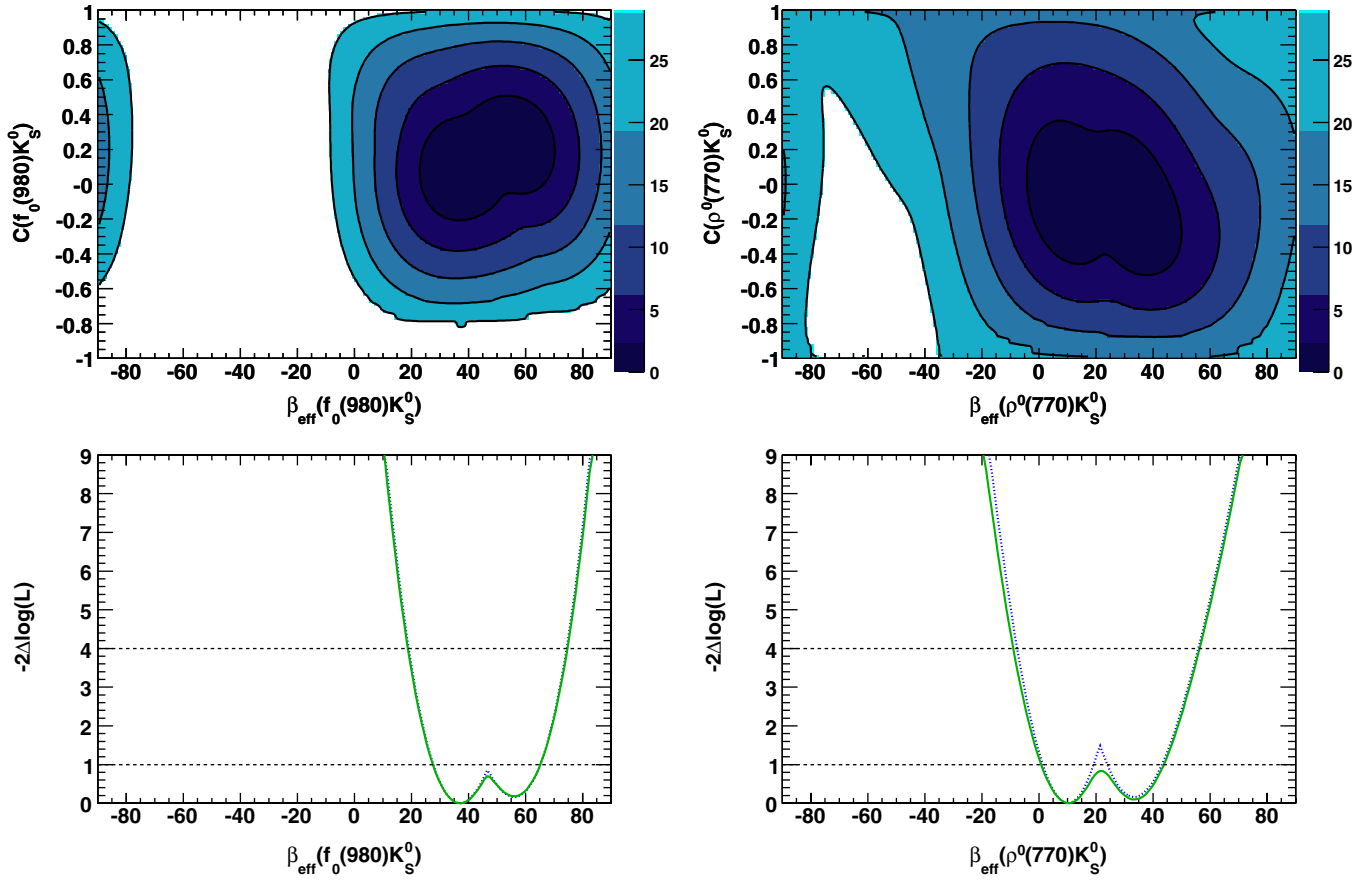

FIG. 9 (color online). Two-dimensional scans of $-2\Delta\log\mathcal{L}$ as a function of β_{eff} and C (top) and the one-dimensional scans as a function of β_{eff} (bottom) for the $f_0(980)K^0_S$ (left) and $\rho^0(770)K^0_S$ (right) isobar components. The value $-2\Delta\log\mathcal{L}$ is computed including systematic uncertainties. On the two-dimensional scans, shaded areas, from the darkest to the lightest, represent the one to five standard deviations contours. The statistical (dashed line), and total (solid line) $-2\Delta\log\mathcal{L}$ are shown on the one-dimensional scans, where horizontal dotted lines mark the one and two standard deviation levels.

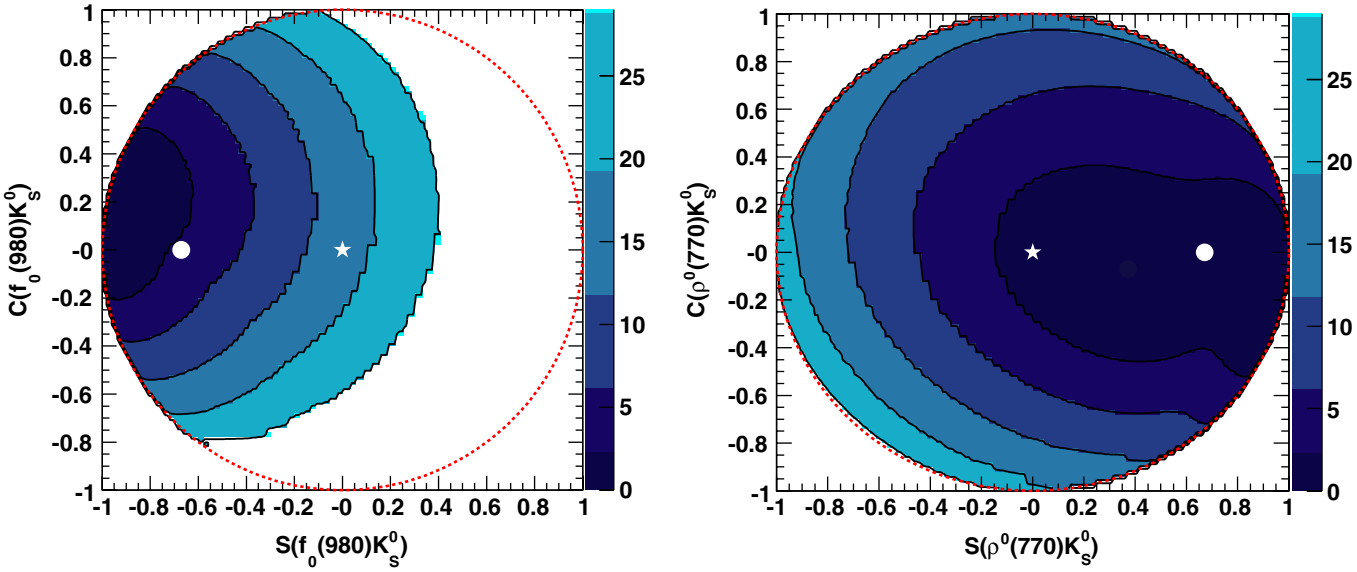

FIG. 10 (color online). Two-dimensional scans of $-2\Delta\log\mathcal{L}$ as a function of (S, C), for the $f_0(980)K^0_S$ (left) and $\rho^0(770)K^0_S$ (right) isobar components. The value $-2\Delta\log\mathcal{L}$ is computed including systematic uncertainties. Shaded areas, from the darkest to the lightest, represent the one to five standard deviations contours. The • (★) marks the expectation based on the current world average from $b \to c\bar{c}s$ modes [3] (zero point). The dashed circle represents the physical border $S^2 + C^2 = 1$.

sentation has nonetheless the advantage of allowing direct comparison with the measurement of sin2β and C in $b \to c\bar{c}s$ modes. For $f_0(980)K^0_S$, the results agree with the expectation based on $b \to c\bar{c}s$ to 1.1σ; for $\rho^0(770)K^0_S$ the agreement is better than 1σ. For the measured values of $(\beta_{\rm eff}, C)$ for $f_0(980)K^0_S$, CP conservation is excluded at 3.5σ. For $\rho^0(770)K^0_S$, the measurement of $(\beta_{\rm eff}, C)$ is consistent with CP conservation within 1σ.

The measurement of the phase $\Delta\Phi(K^{*+}(892)\pi^-)$ is presented as a one-dimensional likelihood scan in Fig. 11. For this flavor-specific mode, there is virtually no region in phase space that is accessible both to B^0 and $\bar{B}^0$; thus, sensitivity to this phase difference is limited. Simulation shows that interference of the $K^{*+}(892)\pi^-$ with the $f_0(980)K^0_S$ and $\rho^0(770)K^0_S$ modes (for which B^0 and $\bar{B}^0$ amplitudes interfere via mixing) provides most of the sensitivity to $\Delta\Phi(K^{*+}(892)\pi^-)$; unfortunately, the overlap in phase space of these resonances is small. As a consequence, only the $[-137, -5]^\circ$ interval is excluded at 95% confidence level. Figure 11 also shows the measurement of the similar phase difference for the $(K\pi)^*_0$ component. As for $K^*(892)$, the measurement sets no strong constraint on this phase. Only the interval $[-132, +25]^\circ$ is excluded at 95% confidence level.

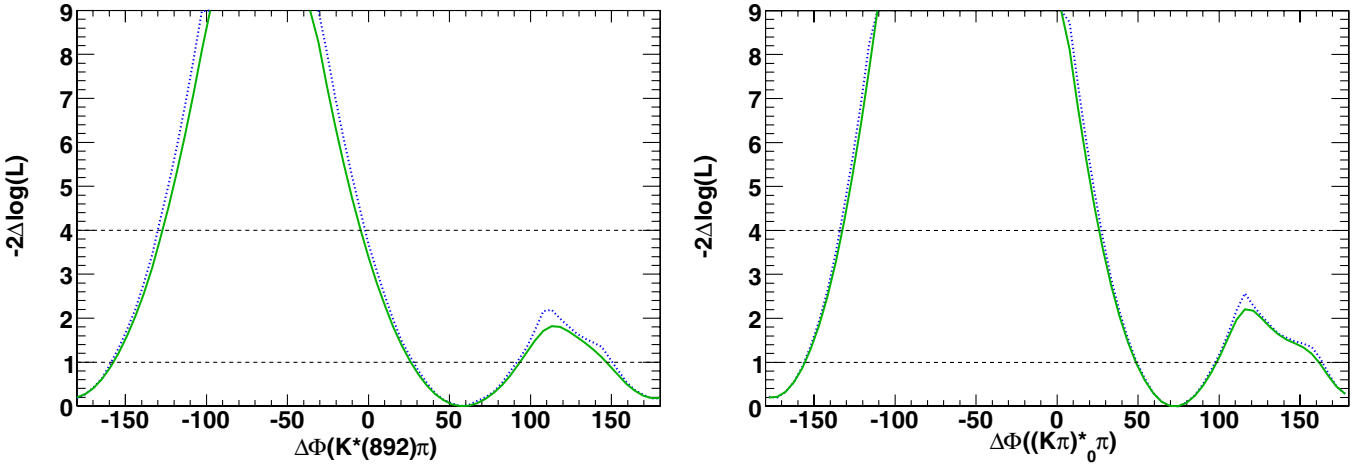

FIG. 11 (color online). Statistical (dashed line) and total (solid line) scans of $-2\Delta\log\mathcal{L}$ as a function of the relative phases $\Delta\Phi(K^*(892)\pi)$ (left) and $\Delta\Phi((K\pi)^*_0)$ (right). Horizontal dotted lines mark the one and two standard deviation levels.

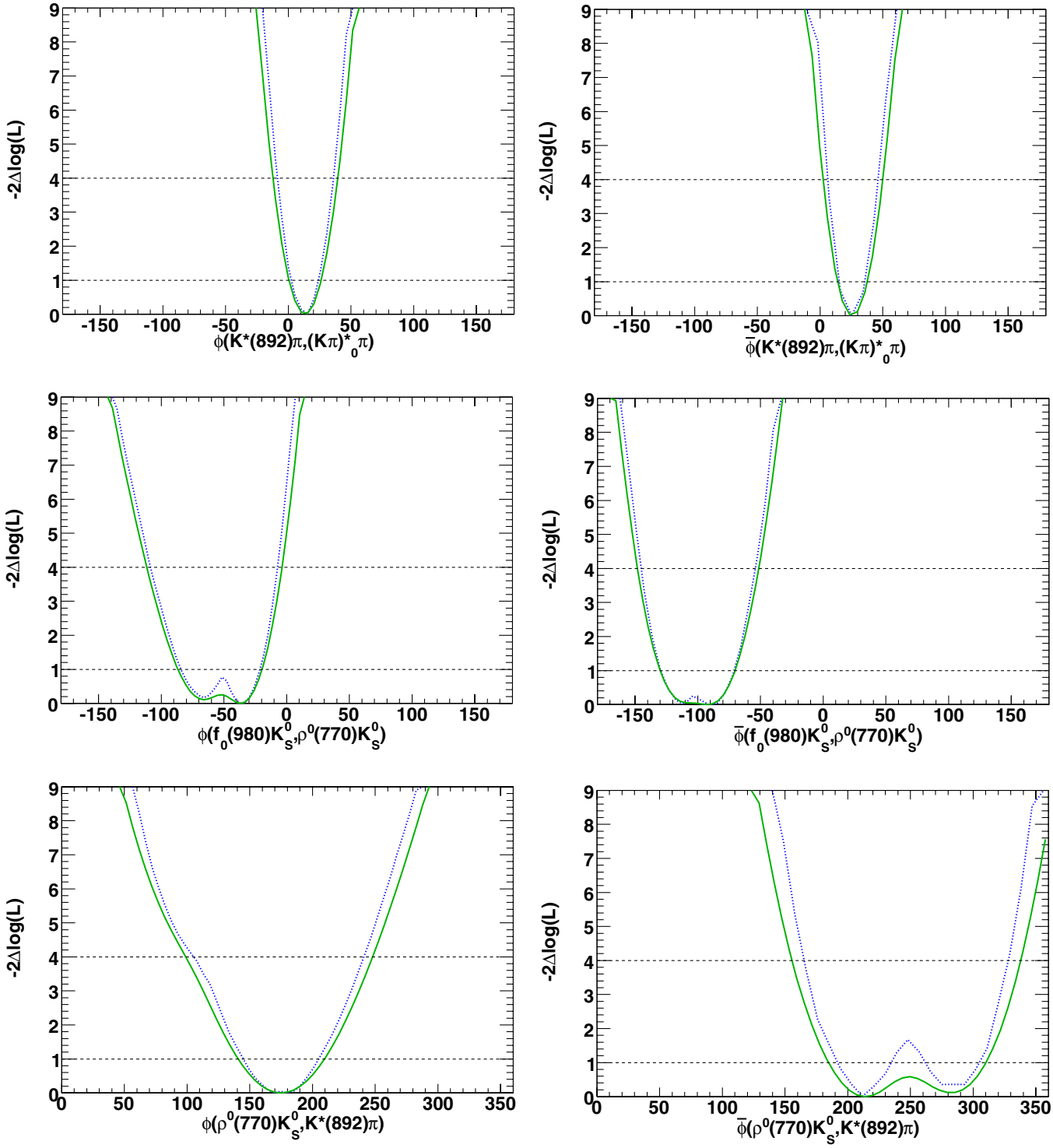

FIG. 12 (color online). Statistical (dashed line) and total (solid line) scans of $-2\Delta\log\mathcal{L}$ as a function of the phase differences $\phi(K^*(892)\pi, (K\pi)^*_0\pi)$ (top), $\phi(f_0(980)K^0_S, \rho^0(770)K^0_S)$ (middle), and $\phi(\rho^0(770)K^0_S, K^*(892)\pi)$ (bottom). The left (right) column shows $B^0(\bar{B}^0)$ candidates. Horizontal dotted lines mark the one and two standard deviation levels.

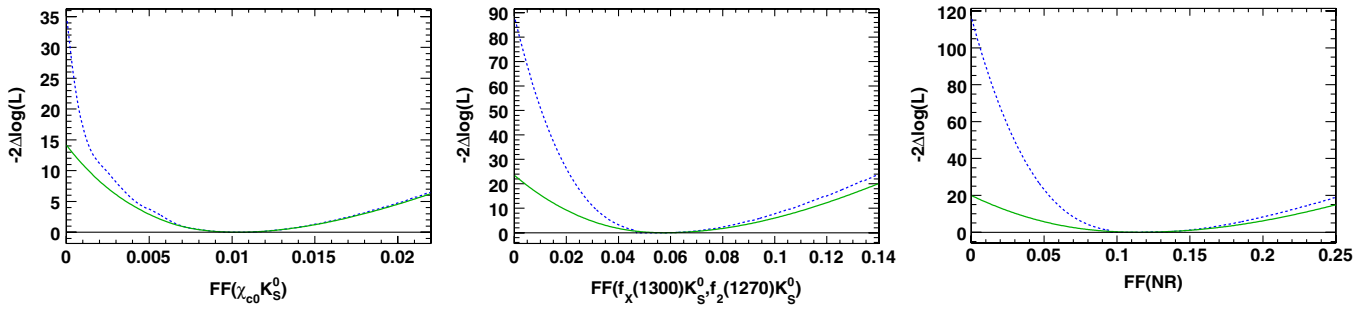

FIG. 13 (color online). Statistical (dashed line) and total (solid line) scans in terms of $-2\Delta\log\mathcal{L}$ as a function of the fit fractions of the $\chi_{c0}(1P)K^0_S$ component (left), the sum of fit fractions of the $f_2(1270)K^0_S$ and $f_X(1300)K^0_S$ components (center), and the flat phase space NR component (right). These scans are used to extract the probability of null values of these fit fractions.

In contrast, due to the sizable overlap in phase space between the $K\pi$ S- and P- waves of the same charge, the relative phases $\phi((K\pi)^{*\pm}_0, K^{*\pm}(892))$ are measured to $\pm 13°$ including systematics. The one-dimensional scans are shown in Fig. 12. The associated observable $\Delta\phi((K\pi)^{*\pm}_0, K^{*\pm}(892))$ is compatible with CP conservation. Figure 12 also shows the scans for $\phi(f_0(980)K^0_S, \rho^0(770)K^0_S)$, $\phi(\rho^0(770)K^0_S, K^{*+}(892)\pi^-)$, and their corresponding CP-conjugates. It is clear from this figure and from Table V that the phases for the former are measured to a better accuracy. This is due to the larger overlap in phase space between the $f_0(980)$ and the $\rho^0(770)$. In both cases the associated observables $\Delta\phi$ are compatible with CP conservation.

For the remaining resonant modes in the signal DP model: $f_X(1300)K^0_S$, $f_2(1270)K^0_S$, NR, and $\chi_{c0}(1P)K^0_S$, we scan the likelihood as a function of the corresponding fit fractions. These scans are shown in Fig. 13. We obtain total (statistical and systematic) significances of 4.8 and 3.8 standard deviations for the NR and $\chi_{c0}(1P)K^0_S$ components, respectively. The significance for the sum of fit fractions of the $f_2(1270)K^0_S$ and $f_X(1300)K^0_S$ components is 4.8 standard deviations while their individual significances are 2.9σ and 2.4σ, respectively.

The $(K\pi)^*_0$ component is modeled in our analysis by the LASS parametrization [35], which consists of a NR effective range term plus a relativistic Breit-Wigner term for the $K^*(1430)$ resonance. We separate from the corresponding branching fraction, quoted in Table VI, the contribution of the $K^*(1430)$ resonance and find it to be $(29.9^{+2.3}_{-1.7} \pm 1.6 \pm 0.6 \pm 3.2) \times 10^{-6}$. This value is corrected for the secondary branching fraction using $\mathcal{B}(K^*(1430) \to K\pi)$ from Ref. [32] and the isospin relation $\mathcal{B}(K^{*+}(1430) \to K^0\pi^+)/\mathcal{B}(K^{*+}(1430) \to K^+\pi^0) = 2$. The first uncertainty is statistical, the second is systematic, the third represents the DP signal model dependence, and the fourth is due to the uncertainty on the secondary branching fraction. In addition, we calculate the total NR contribution by combining coherently the effective range part of the LASS parametrization and the flat phase-space NR component.

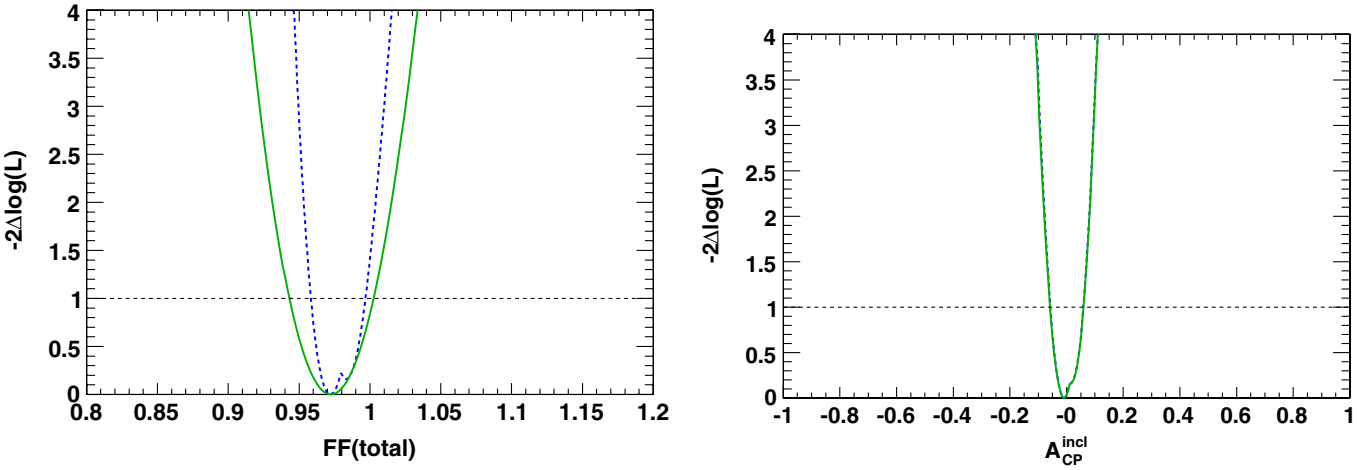

FIG. 14 (color online). Statistical (dashed line) and total (solid line) scans of $-2\Delta\log\mathcal{L}$ as a function of the total fit fraction (left) and the inclusive direct CP-asymmetry $A^{\rm incl}_{CP}$ (right). A horizontal dotted line marks the 1 standard deviation level.

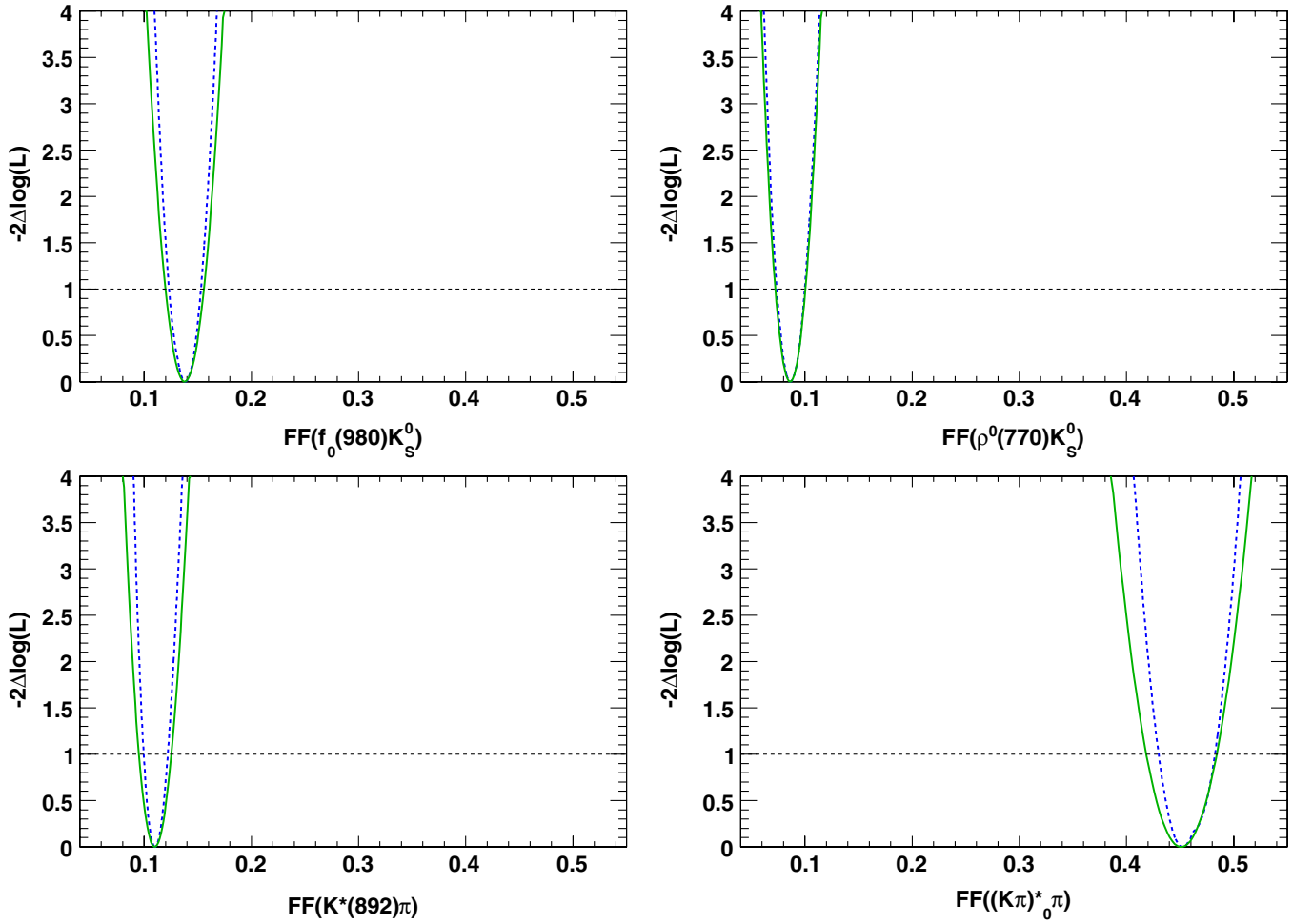

FIG. 15 (color online). Statistical (dashed line) and total (solid line) scans of $-2\Delta\log\mathcal{L}$ as a function of the fit fractions $FF(f_0(980)K_S^0)$ (top left), $FF(\rho^0(770)K_S^0)$ (top right), $FF(K^{*\pm}(892)\pi^{\mp})$ (bottom left), and $FF((K\pi)_0^{*\pm}\pi^{\mp})$ (bottom right). A horizontal dotted line marks the 1 standard deviation level.

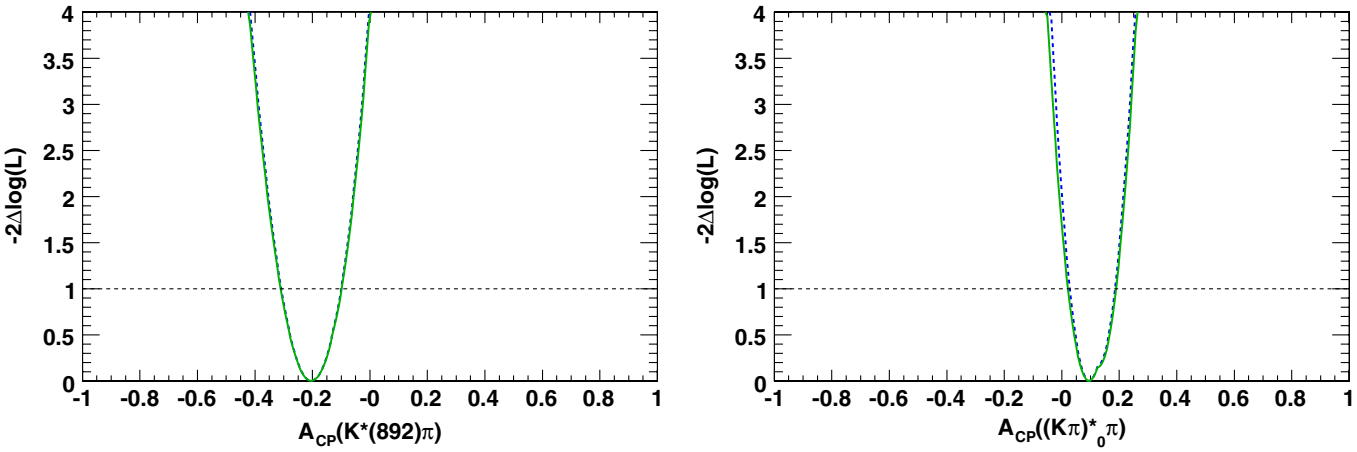

FIG. 16 (color online). Statistical (dashed line) and total (solid line) scans of $-2\Delta\log\mathcal{L}$ as a function of the direct CP asymmetries $A_{CP}(K^{*\pm}(892)\pi^{\mp})$ (left) and $A_{CP}((K\pi)_0^{*\pm}\pi^{\mp})$ (right). A horizontal dotted line marks the 1 standard deviation level.

We find this total NR fit fraction to be $(22.1^{+2.8}_{-2.0} \pm 2.1 \pm 0.7)\%$. Note that this number accounts for the destructive interference between the two NR terms. The corresponding branching fraction is $(11.07^{+2.51}_{-0.99} \pm 0.81 \pm 0.40) \times 10^{-6}$.

Measurements of the $K^*(892)\pi$ and $K^*(1430)\pi$ resonant modes were also made by *BABAR* in the Dalitz plot analysis of the decay $B^0(\bar{B}^0) \to K^\pm\pi^\mp\pi^0$ [26]. Combining the likelihoods from this analysis and the present one we obtain the average branching fractions and *CP* asymmetries for these resonant modes. In the combination, we consider the systematic uncertainties due to the DP model, line shapes, particle identification, tracking efficiency corrections, and the calculation of $N_{B\bar{B}}$ pairs (see Sec. VII) as fully correlated. The rest of the systematic errors are assumed to be uncorrelated. The averages obtained for the $K^*(892)\pi$ resonant mode are $\mathcal{B}(B^0 \to K^{*+}(892)\pi^-) = (9.6 \pm 1.0) \times 10^{-6}$ and $A_{CP}(K^{*+}(892)\pi^-) = -0.197^{+0.092}_{-0.085}$ The quoted result for the branching fraction is averaged over charge conjugate states. It was corrected for the secondary branching fraction using $\mathcal{B}(K^* \to K\pi) = \frac{2}{3}$. The average A_{CP} and branching fraction for the $K^*(1430)\pi$ resonant mode do not differ within the quoted significant digits from the results of the present analysis. This is due to the fact that these quantities suffer from large errors caused by multiple solutions in the $B^0(\bar{B}^0) \to K^\pm\pi^\mp\pi^0$ analysis.

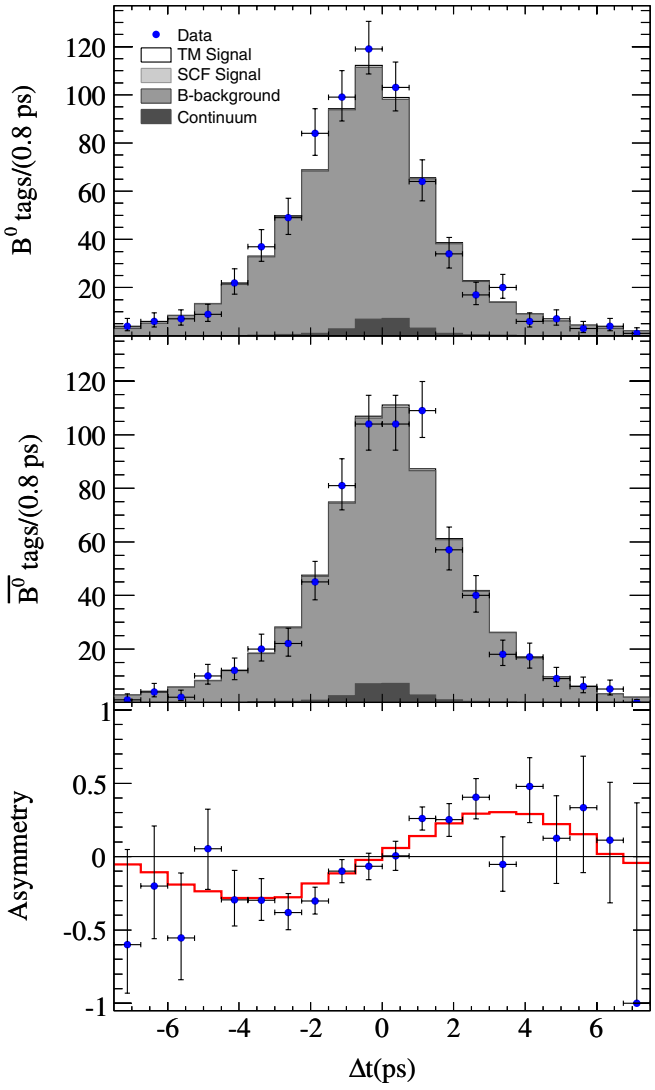

FIG. 17 (color online). Distributions of Δt when the $B^0_{\rm tag}$ is a B^0 (top), $\bar{B}^0$ (middle), and the derived Δt asymmetry (bottom) for events in the $J/\psi K^0_S$ region. The solid line is the total PDF and the points with error bars represent data.

As a validation of our treatment of the time-dependence, we allow τ_{B^0} and Δm_d to vary in the fit. We find $\tau_{B^0} = 1.579 \pm 0.061$ ps and $\Delta m_d = 0.497 \pm 0.035$ ps^{-1} while the remaining free parameters are consistent with the nominal fit. The numbers for τ_{B^0} and Δm_d are in agreement with current world averages [3]. In addition we perform a fit floating the S parameters for $B^0 \to J/\psi K^0_S$ and $B^0 \to \psi(2S)K^0_S$ events. We find $S = \sin(2\beta) = 0.690 \pm 0.077$ and 0.73 ± 0.27 for $J/\psi K^0_S$ and $\psi(2S)K^0_S$ respectively. These numbers are in agreement with the current world average [3]. Signal-enhanced distributions of Δt and the Δt asymmetry for events in the $J/\psi K^0_S$ region are shown in Fig. 17. To validate the SCF modeling, we leave the average SCF fractions per tagging category free to vary in the fit and find results that are consistent with the MC estimation.

As a further cross check of the results, we performed an independent analysis and obtained compatible results [47]. The main differences between this cross-check analysis and the one presented here were the use of a Fisher discriminant instead of a NN, the removal of bands in invariant mass to cut away the $B^0 \to D^-\pi^+$, $B^0 \to J/\psi K^0_S$ and $B^0 \to \psi(2S)K^0_S$ contributions, and the use of Cartesian isobar parameters.

VII. SYSTEMATIC STUDIES

To estimate the contribution to $B^0 \to K^0_S\pi^+\pi^-$ decay via other resonances, we first fit the data including these other decays in the fit model. We consider possible resonances, including $\omega(782)$, $\rho^0(1450)$, $\rho^0(1700)$, $f_0(1710)$, $f_2(1810)$, $K^{*\pm}(1680)$, $K^{*\pm}_2(1430)$, $\chi_{c2}(1P)$, and a low mass σ state. Relativistic Breit–Wigner line shapes are used to parametrize these additional resonances, with masses and widths from Ref. [32]. As a second step we simulate high statistic samples of events, using a model based on the previous fits, including the additional resonances. Finally, we fit these simulated samples using the nominal signal model. The systematic effect (contained in the "DP model" field in Table VII) is taken from the difference observed between the generated and fitted values. We quote this DP model uncertainty separately from other systematics.

We vary the mass, width, and any other parameters of all isobar fit components within their errors, as quoted in

TABLE VII. Summary of systematic uncertainties on Q2B parameters. Errors on relative fractions ($\beta_{\rm eff}$ and phases) are given in percent (degrees).

Parameter	DP model	Line shape	Fit bias	B Background	Other	Total
$C(f_0(980)K^0_S)$	0.04	0.02	<0.01	0.01	0.02	0.05
$FF(f_0(980)K^0_S)$	0.6	0.69	0.5	0.07	<0.01	1.03
$\beta_{\rm eff}(f_0(980)K^0_S)$	2.1	1.9	<0.1	0.2	0.3	2.9
$C(\rho^0(770)K^0_S)$	0.03	0.04	<0.01	0.06	0.06	0.10
$FF(\rho^0(770)K^0_S)$	0.23	0.31	0.3	0.09	0.15	0.52
$\beta_{\rm eff}(\rho^0(770)K^0_S)$	1.8	2.2	<0.1	1.2	1.7	3.5
$A_{CP}(K^*(892)\pi)$	0.02	<0.01	<0.01	<0.01	<0.01	0.02
$FF(K^*(892)\pi)$	0.8	0.13	0.4	0.03	0.43	1.00
$\Delta\Phi(K^*(892)\pi)$	8.1	2.8	<0.1	1.4	3.3	9.3
$A_{CP}((K\pi)^*_0\pi)$	0.02	<0.01	<0.01	<0.01	0.02	0.03
$FF((K\pi)^*_0\pi)$	0.90	0.39	1.8	0.12	0.33	2.08
$\Delta\Phi((K\pi)^*_0\pi)$	4.4	2.4	<0.1	1.3	3.0	6.0
$C(f_2(1270)K^0_S)$	0.07	0.04	<0.01	0.05	0.06	0.11
$FF(f_2(1270)K^0_S)$	0.69	0.16	0.09	0.02	0.19	0.74
$C(f_X(1300)K^0_S)$	0.09	0.03	<0.01	0.01	0.03	0.10
$FF(f_X(1300)K^0_S)$	0.87	0.28	0.14	0.02	0.17	0.94
$C(NR)$	0.04	0.01	<0.01	0.01	0.07	0.08
$FF(NR)$	0.60	0.86	0.5	0.12	1.62	2.00
$C(\chi_{c0}K^0_S)$	0.05	0.02	<0.01	0.01	0.02	0.06
$FF(\chi_{c0}K^0_S)$	0.09	0.06	0.04	<0.01	<0.01	0.11
$A^{\rm incl}_{CP}$	<0.01	<0.01	<0.01	<0.01	0.01	0.01
$FF_{\rm Tot}$	1.15	0.55	2.0	0.08	0.36	2.40
$\phi(f_0(980)K^0_S, \rho^0(770)K^0_S)$	4.4	2.6	<0.1	3.4	4.3	7.5
$\phi(\rho^0(770)K^0_S, K^*(892)\pi)$	12.7	3.0	<0.1	3.6	7.3	15.4
$\phi(\rho^0(770)K^0_S, (K\pi)^*_0\pi)$	8.7	8.5	<0.1	3.9	3.7	13.3
$\phi(K^*(892)\pi, (K\pi)^*_0\pi)$	4.7	0.7	<0.1	0.3	4.6	6.6
Signal Yield	31.7	5.8	14.0	3.3	23.0	42.1

Table I, and assign the observed differences in the measured amplitudes as systematic uncertainties (Line shape in Table VII).

To validate the fitting tool, we perform fits on large MC samples of fully-reconstructed events with the measured proportions of signal, continuum, and B background events. No significant biases are observed in these fits and therefore no corrections are applied. The statistical uncertainties on the fit parameters are taken as systematic uncertainties (''Fit Bias'' in Table VII).

Another major source of systematic uncertainty is the B background model. The expected event yields from the background modes are varied according to the uncertainties in the measured or estimated branching fractions. Since B background modes may exhibit CP violation, the corresponding parameters are varied within their uncertainties, or, if unknown, within the physical range. As is done for the signal PDFs, we vary the Δt resolution parameters and the flavor-tagging parameters within their uncertainties and assign the differences observed in these fits with respect to the nominal fit as systematic errors. These errors are listed as ''B Background '' in Table VII.

Other systematic effects are much less important for the measurements of the amplitudes and are combined in the ''Other'' field in Table VII. Details are given below.

The parameters of the continuum PDFs are determined by the fit. No additional systematic uncertainties are assigned to them. An exception to this is the DP PDF: to estimate the systematic uncertainty from the $m_{\rm ES}$ sideband extrapolation, we use large samples of $e^+e^- \to q\bar{q}$ MC data ($q = u, d, s, c$). We compare the distributions of m' and θ' between sidebands at different ranges in $m_{\rm ES}$ and find the two such sidebands that show the maximum dis-

crepancy. We assign as systematic uncertainty the effect seen when weighting the continuum DP PDF by the ratio of these two data sets.

The uncertainties associated with Δm_d and τ are estimated by varying these parameters within the uncertainties on the world average [32].

The signal PDFs for the Δt resolution and tagging fractions are determined from fits to a control sample of fully reconstructed B decays to exclusive final states with charm, and the uncertainties are obtained by varying the parameters within the statistical uncertainties.

Finally, the uncertainties due to particle identification, tracking efficiency corrections, K^0_S reconstruction, and the calculation of $N_{B\bar{B}}$ are 2.0%, 1.6%, 0.9%, and 1.1%, respectively. Only the branching fractions are affected by these uncertainties; they intervene as a multiplicative factor that affects all the signal modes mostly in the same way, and hence cancels out in the CP measurements. The only residual impact on these is related to detector charge asymmetry, due to which the factors corresponding to B^0 and $\bar{B}^0$ decays are not identical. This effect has been studied and shown to be very small ($< 1\%$) compared to the other sources of systematic error we include. The branching fractions are affected via the total inclusive branching fraction in Eq. (44).

The average fraction of misreconstructed signal events ($\bar{f}_{\rm SCF}$) predicted by the MC simulation has been verified with fully reconstructed $B \to D\rho$ events [42]. No significant differences between data and the simulation were found. To estimate a systematic uncertainty from $\bar{f}_{\rm SCF}$, we vary these fractions, for all tagging categories. Tagging efficiencies, dilutions, and biases for signal events are varied within their experimental uncertainties.

VIII. SUMMARY

We have presented results from a time-dependent Dalitz plot analysis of $B^0 \to K^0_S\pi^+\pi^-$ decays obtained from a data sample of 383×10^6 $\Upsilon(4S) \to B\bar{B}$ decays. Using an amplitude analysis technique, we measure 15 pairs of relative magnitudes and phases for the different resonances, taking advantage of the interference between them in the Dalitz plot. From the measured decay amplitudes, we derive the Q2B parameters of the resonant decay modes. Two solutions, with equivalent goodness-of-fit, were found.

Including systematic and Dalitz plot model uncertainties, the combined confidence interval for the measured values of $\beta_{\rm eff}$ in B^0 decays to $f_0(980)K^0_S$ is $18^\circ < \beta_{\rm eff} < 76^\circ$ at 95% C.L. CP conservation in B^0 decays to $f_0(980)K^0_S$ is excluded at 3.5σ, including systematics. For B^0 decays to $\rho^0(770)K^0_S$, the combined confidence interval is $-9^\circ < \beta_{\rm eff} < 57^\circ$ at 95% C.L. These results are both consistent with the measurements in $b \to c\bar{c}s$ modes.

In decays to $K^{*+}(892)\pi^-$, we find $A_{CP} = -0.20 \pm 0.10 \pm 0.01 \pm 0.02$. We combine this result with that from Ref. [26], and obtain $A_{CP}(K^*(892)\pi) = -0.197^{+0.092}_{-0.085}$. This average is consistent with CP conservation only at the level of 2.4 standard deviations. For the relative phase between decay amplitudes of $B^0 \to K^{*+}(892)\pi^-$ and $\bar{B}^0 \to K^{*-}(892)\pi^+$, we exclude the interval $-137^\circ < \Delta\Phi(K^*(892)\pi) < -5^\circ$ at 95% C.L. This last result, combined with measurements of branching ratios, direct CP asymmetries, and relative phases in $K^{*+}(892)\pi^-$ and $K^{*0}(892)\pi^0$, plus a theoretical hypothesis on the contributions of electroweak penguins to the decay amplitudes, can be used to set nontrivial constraints on the CKM parameters $(\bar{\rho}, \bar{\eta})$ by following the methods proposed in Refs. [18–21].

ACKNOWLEDGMENTS

We are grateful for the extraordinary contributions of our PEP-II colleagues in achieving the excellent luminosity and machine conditions that have made this work possible. The success of this project also relies critically on the expertise and dedication of the computing organizations that support *BABAR*. The collaborating institutions wish to thank SLAC for its support and the kind hospitality extended to them. This work is supported by the U.S. Department of Energy and National Science Foundation, the Natural Sciences and Engineering Research Council (Canada), the Commissariat à l'Energie Atomique and Institut National de Physique Nucléaire et de Physique des Particules (France), the Bundesministerium für Bildung und Forschung and Deutsche Forschungsgemeinschaft (Germany), the Istituto Nazionale di Fisica Nucleare (Italy), the Foundation for Fundamental Research on Matter (The Netherlands), the Research Council of Norway, the Ministry of Education and Science of the Russian Federation, Ministerio de Educación y Ciencia (Spain), and the Science and Technology Facilities Council (United Kingdom). Individuals have received support from the Marie-Curie IEF program (European Union) and the A. P. Sloan Foundation.

APPENDIX

The full (statistical, systematic, and model dependence) correlation matrices of the isobar parameters for solutions I and II are given in Tables VIII and IX, respectively. The tables are organized in blocks for c, $\bar{c}$, arg$c$, and arg$\bar{c}$. Here, the abbreviations f_0, ρ^0, K^*, S, f_2, f_X, NR, and χ represent the components $f_0(980)K^0_S$, $\rho^0(770)K^0_S$, $K^*(892)\pi$, $(K\pi)^*_0\pi$, $f_2(1270)K^0_S$, $f_X(1300)K^0_S$, nonresonant, and $\chi_{c0}K^0_S$, respectively.

TABLE VIII. Full correlation matrix for the isobar parameters of solution I. The entries are given in percent. Since the matrix is symmetric, all elements above the diagonal are omitted.

		$\lvert c\rvert$								$\lvert\bar{c}\rvert$						
		ρ^0	K^*	S	f_2	f_X	NR	χ	f_0	ρ^0	K^*	S	f_2	f_X	NR	χ
$\lvert c\rvert$	ρ^0	100.0														
	K^*	51.9	100.0													
	S	54.0	65.0	100.0												
	f_2	8.4	2.8	21.0	100.0											
	f_X	14.9	23.2	32.2	22.7	100.0										
	NR	5.2	35.0	24.4	12.6	39.3	100.0									
	χ	6.4	9.9	7.8	2.0	7.4	6.1	100.0								
$\lvert\bar{c}\rvert$	f_0	31.3	30.3	39.9	25.2	36.7	31.3	8.0	100.0							
	ρ^0	20.6	48.6	51.2	8.0	27.7	27.5	5.6	17.3	100.0						
	K^*	44.7	73.5	56.3	−4.8	24.9	22.0	9.5	22.6	43.4	100.0					
	S	59.6	71.9	79.7	21.8	39.3	26.9	11.3	35.2	49.4	57.7	100.0				
	f_2	2.4	−10.1	6.3	−56.1	−1.5	3.9	−0.3	10.7	−6.2	−21.5	5.0	100.0			
	f_X	14.5	34.1	12.5	16.1	−23.0	12.4	2.5	34.5	7.3	8.3	12.9	−6.2	100.0		
	NR	17.8	57.6	41.7	12.7	10.1	49.7	2.4	40.0	32.1	25.0	31.7	7.5	46.2	100.0	
	χ	18.9	27.0	30.6	5.8	11.8	9.5	−84.2	21.5	17.8	24.1	27.8	0.8	8.1	20.2	100.0
$\arg(c)$	ρ^0	−11.2	13.3	4.0	−16.1	−2.9	−2.1	−0.5	−0.2	24.1	16.3	3.2	−3.3	8.9	2.1	4.2
	K^*	25.0	8.6	−3.2	−0.2	−15.7	−9.7	6.3	−10.4	−3.9	5.5	16.0	3.8	6.3	−6.5	−3.2
	S	33.0	19.6	3.4	−4.7	−17.3	−16.5	6.2	−9.6	1.0	18.7	21.3	−4.2	9.6	−4.2	1.1
	f_2	12.1	−0.6	−9.8	−2.6	−23.1	−27.4	0.9	−16.7	−7.2	2.2	1.1	−10.6	7.2	−14.1	−2.6
	f_X	25.0	10.2	5.4	−0.5	−11.4	−11.8	1.0	−0.8	2.6	8.5	11.8	−3.8	15.6	2.4	0.4
	NR	31.6	17.0	39.3	1.0	−27.1	−31.7	−6.7	11.3	12.8	14.5	19.0	3.3	21.5	19.6	14.2
	χ	8.6	1.8	9.8	0.6	−9.9	−8.9	−7.9	2.8	3.8	1.3	4.2	3.5	7.3	8.9	12.4
$\arg(\bar{c})$	f_0	32.2	11.7	18.9	3.5	−20.3	−26.2	−1.6	−3.6	−6.9	7.3	18.2	1.8	20.3	−7.1	4.3
	ρ^0	14.5	18.0	14.6	−17.3	−13.4	−21.0	−0.7	−8.7	14.3	19.8	13.4	1.7	7.2	−4.4	5.4
	K^*	17.1	7.1	22.0	5.2	−13.5	−17.3	−2.1	5.0	7.2	6.5	13.8	8.1	12.8	29.5	9.6
	S	22.5	15.9	25.2	−3.2	−16.9	−21.6	−0.5	4.2	10.6	17.7	16.1	1.7	14.1	28.8	10.8
	f_2	15.1	4.9	15.5	−5.0	−15.5	−17.9	−2.1	10.0	−2.5	3.9	2.9	11.1	15.7	18.6	7.5
	f_X	8.1	2.7	12.3	−0.6	16.5	−20.4	−0.9	12.2	6.1	3.4	4.8	1.4	−14.6	4.7	6.5
	NR	15.3	4.1	14.5	−3.0	−22.6	−20.8	0.8	1.7	8.2	1.8	5.2	2.6	20.0	15.1	3.2
	χ	10.9	1.1	12.8	0.7	−13.9	−18.0	−4.7	2.1	3.3	0.6	3.9	5.9	9.8	13.4	8.2

		$\arg(c)$								$\arg(\bar{c})$						
		ρ^0	K^*	S	f_2	f_X	NR	χ	f_0	ρ^0	K^*	S	f_2	f_X	NR	χ
$\arg(c)$	ρ^0	100.0														
	K^*	10.4	100.0													
	S	18.2	90.9	100.0												
	f_2	19.6	54.1	61.8	100.0											
	f_X	25.5	49.3	56.9	58.1	100.0										
	NR	24.3	17.2	29.9	31.6	47.8	100.0									
	χ	5.0	6.7	7.9	10.2	17.6	30.8	100.0								
$\arg(\bar{c})$	f_0	18.0	34.3	42.0	39.8	52.9	55.6	23.8	100.0							
	ρ^0	55.3	22.2	32.4	25.7	36.6	42.2	17.4	58.8	100.0						
	K^*	4.0	21.5	28.0	23.2	36.1	53.9	31.3	46.8	33.5	100.0					
	S	9.6	23.7	35.1	27.8	41.2	60.7	33.3	53.4	42.7	90.9	100.0				
	f_2	5.5	6.4	12.4	1.5	29.3	46.4	23.5	44.1	36.7	56.7	60.8	100.0			
	f_X	1.7	0.0	5.4	13.8	15.5	36.4	19.5	22.2	22.5	42.1	44.8	39.4	100.0		
	NR	7.2	19.2	27.5	28.9	42.3	55.5	32.9	47.3	37.9	63.2	72.5	48.1	48.4	100.0	
	χ	4.1	8.9	13.3	15.5	27.1	43.3	35.9	38.0	26.9	55.9	58.9	40.0	33.6	52.1	100.0

TABLE IX. Full correlation matrix for the isobar parameters of solution II. The entries are given in percent. Since the matrix is symmetric, all elements above the diagonal are omitted.

		$\lvert c\rvert$								$\lvert\bar{c}\rvert$						
		ρ^0	K^*	S	f_2	f_X	NR	χ	f_0	ρ^0	K^*	S	f_2	f_X	NR	χ
$\lvert c\rvert$	ρ^0	100.0														
	K^*	46.9	100.0													
	S	49.1	68.2	100.0												
	f_2	8.7	7.7	25.4	100.0											
	f_X	16.8	40.3	38.5	26.6	100.0										
	NR	−8.4	30.2	21.2	9.4	49.9	100.0									
	χ	5.5	11.7	9.3	3.4	12.1	9.1	100.0								
$\lvert\bar{c}\rvert$	f_0	29.2	42.1	50.2	31.5	57.9	34.1	10.0	100.0							
	ρ^0	61.5	68.1	40.4	6.9	20.6	6.4	6.0	31.6	100.0						
	K^*	39.8	75.7	59.8	0.3	33.1	25.3	10.9	33.2	36.3	100.0					
	S	50.6	75.2	83.2	25.4	49.9	33.4	13.1	51.6	46.0	61.4	100.0				
	f_2	0.8	−6.1	9.6	−53.9	6.0	13.3	0.2	14.7	5.3	−18.5	10.4	100.0			
	f_X	10.0	−3.3	−0.9	−10.6	−68.7	−17.8	−5.2	−18.4	6.3	−4.0	−4.9	2.2	100.0		
	NR	23.1	68.8	44.7	13.5	39.3	34.4	5.8	45.6	58.3	32.8	45.4	14.7	−13.8	100.0	
	χ	22.3	33.5	37.8	9.8	19.3	9.9	−79.2	31.3	20.7	30.2	36.1	3.3	−2.6	23.3	100.0
$\arg(c)$	ρ^0	−23.1	13.7	5.5	−11.4	8.0	5.2	0.0	9.0	−11.9	14.5	6.3	−0.2	0.3	3.8	6.9
	K^*	30.6	2.0	−2.2	−6.3	−16.1	−28.1	−0.0	−15.2	14.3	−1.4	6.1	2.0	19.4	−10.3	0.5
	S	38.1	8.9	1.8	−10.1	−17.9	−39.5	−0.1	−15.8	17.4	9.4	7.7	−8.2	19.7	−12.1	3.7
	f_2	18.1	−10.0	−13.7	−7.4	−15.4	−41.3	−2.4	−18.6	1.0	−6.2	−10.2	−12.7	10.7	−21.6	−2.7
	f_X	26.2	−7.8	−12.2	−5.9	−7.7	−35.9	−1.7	−14.5	7.8	−5.7	−8.8	−9.9	12.2	−15.2	−3.6
	NR	32.4	−0.4	21.4	0.5	−29.5	−65.2	−10.4	−4.2	12.0	0.2	0.4	−6.4	21.2	−8.1	10.2
	χ	15.4	−2.2	0.2	−1.6	−9.9	−18.3	−4.9	−5.6	5.6	−3.0	−0.2	−0.8	9.2	−5.6	4.0
$\arg(\bar{c})$	f_0	30.1	−8.0	−2.3	−0.9	−13.2	−43.0	−2.8	−16.7	12.1	−7.2	−5.5	−4.9	10.4	−18.7	−1.6
	ρ^0	7.6	11.4	5.8	−7.5	−1.8	−24.7	0.6	−7.5	4.1	15.1	5.5	−12.6	1.3	−7.0	4.0
	K^*	27.0	0.8	7.6	5.6	2.8	−27.8	0.6	−2.0	9.1	1.5	7.1	3.2	−6.9	13.9	4.1
	S	32.6	8.0	8.4	−1.1	0.6	−31.3	2.1	−4.1	12.6	12.1	7.6	−5.6	−4.4	12.2	4.7
	f_2	18.7	1.7	6.6	10.1	9.8	−22.9	0.7	7.6	8.6	3.5	0.6	−5.6	−21.6	9.3	4.6
	f_X	21.9	1.8	4.4	9.6	−0.7	−30.2	0.1	−5.0	8.1	2.8	4.0	−17.3	1.0	−6.6	−0.2
	NR	27.7	−1.9	−3.0	3.9	−0.5	−30.7	2.8	−13.3	7.8	−1.5	−1.2	−13.8	−7.2	−3.7	−5.0
	χ	19.7	−5.0	−0.5	2.3	−4.4	−27.6	2.7	−6.1	6.2	−4.1	−2.5	−1.6	−0.2	−0.1	−2.9

		$\arg(c)$								$\arg(\bar{c})$						
		ρ^0	K^*	S	f_2	f_X	NR	χ	f_0	ρ^0	K^*	S	f_2	f_X	NR	χ
$\arg(c)$	ρ^0	100.0														
	K^*	2.9	100.0													
	S	7.4	90.6	100.0												
	f_2	9.9	56.6	65.5	100.0											
	f_X	5.9	57.0	64.4	69.5	100.0										
	NR	10.1	37.0	50.3	44.4	46.6	100.0									
	χ	2.6	39.3	40.3	29.1	31.3	28.6	100.0								
$\arg(\bar{c})$	f_0	−0.6	45.8	53.5	47.1	61.0	51.9	27.4	100.0							
	ρ^0	41.3	29.5	39.2	31.2	39.1	33.0	16.5	54.9	100.0						
	K^*	−11.6	35.2	39.7	30.4	42.7	30.0	17.6	56.0	32.9	100.0					
	S	−8.7	38.8	47.7	36.1	49.1	33.7	19.5	62.4	41.1	91.1	100.0				
	f_2	−5.4	12.2	17.9	7.0	28.5	27.2	9.9	52.8	42.0	59.3	61.6	100.0			
	f_X	−7.0	23.2	28.6	28.0	34.4	29.9	15.4	34.6	30.2	43.3	47.1	41.5	100.0		
	NR	−9.0	41.4	47.9	44.2	59.5	30.9	25.2	68.9	48.1	68.6	77.6	54.6	55.8	100.0	
	χ	−7.3	29.3	33.3	28.8	38.8	29.9	8.8	47.1	26.9	54.7	58.0	38.6	35.8	54.6	100.0

[1] N. Cabibbo, Phys. Rev. Lett. **10**, 531 (1963).
[2] M. Kobayashi and T. Maskawa, Prog. Theor. Phys. **49**, 652 (1973).
[3] E. Barberio *et al.* (Heavy Flavor Averaging Group-HFAG), arXiv:0808.1297.
[4] Y. Grossman, Z. Ligeti, Y. Nir, and H. Quinn, Phys. Rev. D **68**, 015004 (2003).
[5] M. Gronau, Y. Grossman, and J. L. Rosner, Phys. Lett. B **579**, 331 (2004).
[6] M. Gronau, J. L. Rosner, and J. Zupan, Phys. Lett. B **596**, 107 (2004).
[7] H.-Y. Cheng, C.-K. Chua, and A. Soni, Phys. Rev. D **72**, 014006 (2005).
[8] M. Gronau and J. L. Rosner, Phys. Rev. D **71**, 074019 (2005).
[9] M. Beneke, Phys. Lett. B **620**, 143 (2005).
[10] G. Engelhard, Y. Nir, and G. Raz, Phys. Rev. D **72**, 075013 (2005).
[11] H.-Y. Cheng, C.-K. Chua, and A. Soni, Phys. Rev. D **72**, 094003 (2005).
[12] A. R. Williamson and J. Zupan, Phys. Rev. D **74**, 014003 (2006).
[13] T. Gershon and M. Hazumi, Phys. Lett. B **596**, 163 (2004).
[14] A. Garmash *et al.* (Belle), Phys. Rev. D **69**, 012001 (2004).
[15] B. Aubert *et al.* (*BABAR*), Phys. Rev. Lett. **99**, 161802 (2007).
[16] L. Wolfenstein, Phys. Rev. Lett. **51**, 1945 (1983).
[17] A. J. Buras, M. E. Lautenbacher, and G. Ostermaier, Phys. Rev. D **50**, 3433 (1994).
[18] N. G. Deshpande, N. Sinha, and R. Sinha, Phys. Rev. Lett. **90**, 061802 (2003).
[19] M. Ciuchini, M. Pierini, and L. Silvestrini, Phys. Rev. D **74**, 051301(R) (2006).
[20] M. Gronau, D. Pirjol, A. Soni, and J. Zupan, Phys. Rev. D **75**, 014002 (2007).
[21] H. J. Lipkin, Y. Nir, H. R. Quinn, and A. E. Snyder, Phys. Rev. D **44**, 1454 (1991).
[22] J. Dalseno *et al.* (Belle), Phys. Rev. D **79**, 072004 (2009).
[23] B. Aubert *et al.* (*BABAR*), Phys. Rev. D **73**, 031101 (2006).
[24] A. Garmash *et al.* (Belle), Phys. Rev. D **75**, 012006 (2007).
[25] P. Chang *et al.* (Belle), Phys. Lett. B **599**, 148 (2004).
[26] B. Aubert *et al.* (*BABAR*), Phys. Rev. D **78**, 052005 (2008).
[27] B. Aubert *et al.* (*BABAR*), Phys. Rev. D **78**, 012004 (2008).
[28] A. Garmash *et al.* (Belle), Phys. Rev. Lett. **96**, 251803 (2006).
[29] Q. Chang, X.-Q. Li, and Y.-D. Yang, J. High Energy Phys. 09 (2008) 038.
[30] J. Blatt and V. E. Weisskopf, *Theoretical Nuclear Physics* (J. Wiley, New York, 1952).
[31] M. Ablikim *et al.* (BES), Phys. Lett. B **607**, 243 (2005).
[32] C. Amsler *et al.* (Particle Data Group), Phys. Lett. B **667**, 1 (2008).
[33] S. M. Flatte, Phys. Lett. B **63**, 224 (1976).
[34] G. J. Gounaris and J. J. Sakurai, Phys. Rev. Lett. **21**, 244 (1968).
[35] D. Aston *et al.* (LASS), Nucl. Phys. **B296**, 493 (1988).
[36] D. V. Bugg, Phys. Lett. B **572**, 1 (2003).
[37] B. Aubert *et al.* (*BABAR*), Phys. Rev. D **72**, 052002 (2005).
[38] B. Aubert *et al.* (*BABAR*), Nucl. Instrum. Methods Phys. Res., Sect. A **479**, 1 (2002).
[39] P. Gay, B. Michel, J. Proriol, and O. Deschamps (1995), prepared for 4th International Workshop on Software Engineering and Artificial Intelligence for High-energy and Nuclear Physics (AIHENP 95), Pisa, Italy, 1995.
[40] B. Aubert *et al.* (*BABAR*), Phys. Rev. Lett. **94**, 161803 (2005).
[41] S. Gardner and J. Tandean, Phys. Rev. D **69**, 034011 (2004).
[42] B. Aubert *et al.* (*BABAR*), Phys. Rev. D **76**, 012004 (2007).
[43] T. Skwarnicki, Ph.D. thesis, DESY-F31-86-02, 1986, Appendix E.
[44] M. Oreglia, Ph.D. thesis, SLAC-R-0236, 1980, Appendix D.
[45] J. Gaiser, Ph.D. thesis, SLAC-R-0255, 1982, Appendix F.
[46] H. Albrecht *et al.* (ARGUS), Z. Phys. C **48**, 543 (1990).
[47] P. del Amo Sanchez, Ph.D. thesis, *BABAR*-THESIS-07-007 (2007).